Metalorganic chemical vapor deposition of aluminum oxides: A paradigm on the process-structure-properties relationship

Constantin Vahlas, Brigitte Caussat

To cite this version:

Constantin Vahlas, Brigitte Caussat. Metalorganic chemical vapor deposition of aluminum oxides: A paradigm on the process-structure-properties relationship. P. Dimitrakis, I. Valov et S. Tappertzhofen. Metal Oxides for Non-volatile Memory: Materials, Technology and Applications, Elsevier, pp.133-168, 2022, ⟨10.1016/b978-0-12-814629-3.00005-2⟩. ⟨hal-04740970⟩

HAL Id: hal-04740970

https://hal.science/hal-04740970v1

Submitted on 17 Jan 2025

Metalorganic chemical vapor deposition of aluminum oxides: A paradigm on the process-structure-properties relationship.

Constantin Vahlas[1], Brigitte Caussat[2]

[1]CIRIMAT-CNRS, Toulouse, France
[2]LGC-CNRS, Toulouse, France

Abstract

This chapter introduces the complex relationships existing among the process conditions, the microstructure and the functional properties for metal oxide films processed by metalorganic chemical vapor deposition. Amorphous aluminum oxide films are considered as a model material due to their promising barrier properties for various applications including non-volatile memories and to the extended investigation of the process and the material. The first part of the chapter considers modeling and simulation aspects of the metal-organic chemical vapor deposition (MOCVD) process with the aim to conformally cover non line of sight surfaces. The second part establishes the relationship between short range order in the films and their barrier properties.

Keywords : Aluminum oxide; MOCVD; kinetic models; CFD; complex substrates; microstructure; short range order; barrier properties

Introduction

The stiffness, hardness and chemical inertia of amorphous aluminum oxide (Al_2O_3) thin films, combined with their optical transmittance make them a key player in several applications including microelectronics, optics, catalysis, protection against corrosion and high temperature oxidation. In particular, it was reported that, in contrast to doped polycrystalline hafnium dioxide HfO_2, amorphous Al_2O_3 films possess the advantages of often low process temperature and operating frequencies up to ~GHz, which enable multi-gate non-volatile field-effect transistor (NVFET) with nanometerscale fin pitch [1-3]. Furthermore, combination of Al_2O_3 with other oxides such as HfO_2 results in high-*k* dielectric layers that exhibit high thermal stability, large band gap and high barrier for oxygen diffusion [4], while the thickness of such films can be assessed towards improving the ferroelectric performance of the device [5]. These advantages allow fabricating non-volatile resistive memory devices on thermally sensitive supports such as paper [6] or polyethylene napthalate [3].

Overall, the number of reports on the preparation of alumina films is significant using either physical vapor deposition (PVD) or chemical (atomic layer deposition, ALD, chemical vapor deposition, CVD) techniques. A practical way to produce amorphous alumina films is metal-organic CVD (MOCVD),[7-12] in which a controlled amount of metal-organic precursor carried over a surface decomposes and reacts to form a conformal condensate thin film.

MOCVD is a potentially attractive technique for processing of such coatings, especially on complex-in-shape temperature sensitive substrates. It allows depositing thin films on heated substrates, by the transport in the reactor of gaseous reactive molecules and then the occurrence of gas phase and surface chemical reactions leading to the formation of the film. CVD processes in general are of industrial interest offering a variety of coating compositions and morphologies to answer severe technological specifications, such as anti-corrosion or catalytic conformal deposits on complex surfaces, under the form of either thin films or nanomaterials (particles, tubes, wires). To overcome drawbacks of thermal incompatibility with the substrate and risks of manipulations of corrosive effluents, MOCVD processes have been developed at relatively low temperature involving liquid or solid metalorganic precursors. Composition, nature of deposited phases, stoichiometry, crystallinity and microstructure of the material can be adjusted by finely tuning the MOCVD operating parameters. However, MOCVD processes are rather difficult to develop and optimize, due to the complicated decomposition mechanisms of thermally sensitive molecular compounds in the gas phase and on the growing surface. The chemistry is often hard to catch due to the difficulty to implement non-intrusive metrology for the *in situ* monitoring of the process. Process numerical modelling allows correlating the local behavior of the MOCVD reactor parameters like the gas flow, temperature, concentration and deposition rate profiles with the reactor geometry and deposition parameters. When available, such models are a valuable tool to optimize a MOCVD process in terms of film thickness and composition, in particular on complex substrates, like micro-patterned silicon wafers, porous membranes or foams or hollow objects like vials. However, the bottleneck is often the knowledge of the chemical reactions and of the associated kinetic laws leading to the film formation.

Because of the previously mentioned well-known technological interest of alumina thin films in various domains, including catalysis, corrosion protection, and electrical insulation, insight into the influence of the MOCVD process on the atomic structure of the ceramic is a valuable key to process and property optimization. Indeed, the development of materials with such superior properties is strongly linked to the understanding of their atomic structure dictated by the fabrication process. This has been illustrated for amorphous alumina films concerning, for example, the corrosion resistance measured by electrochemical impedance spectroscopy[7] or their superior mechanical properties (hardness and Young's modulus).[12] It is therefore crucial to obtain comprehensive insights regarding the influence of a synthesis process on the material composition and atomic structure.

The methodology used to develop a set of chemical reactions and kinetic laws is presented in a first part, together with the capability of a numerical model to help optimizing a MOCVD process on complex substrates. The particular case of an amorphous aluminum oxide deposit on glass vials is described.

The second part is dedicated to the experimental analysis of the interplay existing between the amorphous alumina deposition conditions, the microstructure and local atomic organization of the thin films and their barrier properties against oxidation or biofouling.

I. Process kinetic modeling and simulation of the MOCVD of metal oxides: the case of Al_2O_3 films.

CVD processes are subjected to a strong interplay between the complex reactive transport phenomena occurring inside the reactor and the film characteristics in terms of thickness, composition and even morphology and microstructure.[13] With the increasingly severe specifications regarding film properties, thickness and composition uniformities on always more complex 3D substrates, the empirical development of CVD processes is no more efficient. This is particularly true in the fields of microelectronics, photovoltaics, (microelectromechanical systems) MEMS and thermal barrier and anticorrosion coatings.[13-15]

Computational Fluid Dynamics (CFD) models of CVD reactors associated with the appropriate kinetics laws of gas phase and surface chemical reactions allow to calculate the local profiles of gas flow, temperature, species concentration and deposition rates, as a function of the reactor and substrate geometry and of the deposition parameters. This corresponds to a purely continuous approach at a macroscopic scale. When combined with experimental studies, such models allow accurately analyzing the interplay between the reactive transport phenomena and the film thickness and composition, in order de develop and optimize new CVD processes with high capabilities.

The governing equations that describe the transport phenomena occurring inside a CVD reactor include the conservation of mass, momentum, energy and chemical species, associated with the kinetic laws of the homogeneous and heterogeneous chemical reactions. These equations are implemented in standard CFD codes such as Comsol, Fluent/Ansys, CFX among others. [13-15] However, the kinetic laws are rarely known for CVD processes and their establishment is the real bottleneck of this field. This is particularly true for MOCVD processes involving complex metalorganic precursor molecules, which are decomposed in the gas phase in numerous unknown by-products themselves likely to contribute to the formation of the film.

The methodology used to develop these kinetic laws is empirical. It combines (i) literature data on the reaction mechanisms and on deposition experiments, (ii) dedicated experiments providing the deposition rate and the chemical composition of the film and when possible, the gas phase composition at the exit of the reactor measured by gas chromatography – mass spectrometry (GC-MS) or other analytical techniques, for various operating conditions, and (iii) simulation work using apparent homogeneous and heterogeneous chemical reactions and kinetic laws, developed and optimized by trial and error from (i) and (ii). These apparent reactions represent in a simplified way the complex and numerous real reactions, which are difficult to precisely determine. It must be emphasized that, as they are only global and apparent, they are only valid for the studied range of deposition conditions.

The capability of such approach is detailed below for the MOCVD of amorphous Al_2O_3 films deposited at moderate temperature (350-500°C) and low pressure from aluminum tri-isopropoxide (ATI) diluted in N_2, first on planar[16] and then on complex substrates.[17] The CFD code used is first presented with its main assumptions and boundary conditions. Then, a bibliographic analysis is performed about the available chemical mechanisms and kinetic data, followed by the description of the development of the kinetic model and its validation using experimental results obtained on planar substrates. Finally, the model is applied for the optimization of an original MOCVD reactor dedicated to coat the internal surface of a complex part, namely a glass vial.

1. Model characteristics

The CFD code Fluent 16.2 (Ansys) was used for the works reported in this chapter. Fluent is a pressure-based, implicit Reynolds Averaged Navier Stokes solver that employs a cell-centered finite volume scheme having second-order spatial accuracy. It discretizes any computational domain into elemental control volumes, and permits the use of quadrilateral or hexahedral, triangular or tetrahedral and hybrid meshes. The following assumptions were made:

- Steady state conditions,
- Laminar gas flow (Reynolds number lower than 1000),
- Compressible ideal gas (Mach number of max. 1.4),
- No consideration of the precursor in the evaluation of the physical properties of the inlet gas, and no effect of the heats of reaction, due to the high precursor dilution.

The associated boundary conditions are the following:

- At the gas inlet, a flat profile was imposed on the gas velocity, and the mass flow rate and species mass fractions were fixed in accordance with the process conditions.
- At the symmetry axis and at the exit, classical Danckwerts conditions (diffusive flux densities equal to zero), were applied for gas velocity and mass fractions.
- On the walls and substrate surfaces, a classical no-slip condition was used for the gas velocity; the mass flux density of each species was assumed to be equal to the corresponding heterogeneous reaction rate.
- At the exit, the total pressure was fixed at the experimental value.

The physical properties of the gaseous species and the multicomponent diffusion coefficients were calculated using the kinetic theory of gases and the Chapman-Enskog theory, respectively[18]. Lennard-Jones parameters for N_2, O_2 and H_2O were taken from the FLUENT database. The Lennard Jones parameters for C_6H_{12} and C_3H_6 were taken from Bird et al.[18]. These parameters are unknown for ATI and were considered the same as those of n-decane, this molecule having almost the same number of carbon atoms. The ATI molar fraction being low, a small error on these values did not affect the simulation results.

2. Bibliographic analysis on the chemical mechanisms and kinetic laws

Some groups worked on the Al_2O_3 MOCVD process from ATI. Kawase et al. [19] developed a CVD rate analysis method by using non-isothermal tubular reactors of small diameter (1.6 - 5 mm) for alumina deposition from ATI. Since the gas composition can be kept practically constant in the thin tubular reactor, the deposition rate can be measured simultaneously at various temperatures[20]. Working at temperatures higher than 800°C and at 4 kPa of total pressure, they found that gas phase reactions control the deposition-rate and that the ATI decomposition rate is first order with respect to the ATI concentration. They mention that Barybin and Tomilin [21] reported the following overall reaction:

$2\ Al(i\text{-}OC_3H_7)_3 \rightarrow Al_2O_3 + 3\ C_3H_7OH + 3\ C_3H_6$ (R1)

and that Pauer et al.[22] reported:

$2\ Al(i\text{-}OC_3H_7)_3 \rightarrow Al_2O_3 + 3\ (C_3H_7)_2O$ (R2)

$(C_3H_7)_2O \rightarrow 2\ C_3H_6 + H_2O$ (R3)

Hofman et al. [23] performed mass spectroscopic experiments at the exit of a hot wall CVD reactor operating at 400 Pa between 220 °C and 450 °C. The authors found that the deposition kinetics is a second order process, explained by the fact that the rate-limiting step is dehydration of the deposited AlOOH into Al_2O_3. They also showed that deposition by-products are propene, water and 2-propanol, in agreement with Pauer et al.[22].

Blittensdorf et al.[24] used a stagnation point cold wall CVD reactor to investigate the alumina deposition rate from ATI/O_2/Ar mixtures between 350 °C and 1,080 °C and 5-25 kPa total pressure. The aim was to minimize gas phase reactions in order to mainly analyze the heterogeneous reactions. They found a deposition rate independent of temperature at 10 kPa. They attributed this behavior to the fact that the process was operated in the transport-limited regime, meaning that the transition temperature between a surface to a transport limited regime occurs at temperatures below 400 °C. This result is in agreement with that of Saraie et al.[25] who found that the temperature of the transition regime increased from 270 to 350°C with the ATI concentration in the inlet gas. These authors[25] experimentally studied the influence of various atmospheres (N_2, N_2/O_2, N_2/H_2, N_2/H_2O) on the deposition rate of alumina from ATI in a hot wall reactor between 200 °C and 350 °C at a total pressure 2 kPa and proposed an activation energy of 80 kJ/mol. Kim et al.[26] studied the deposition of alumina on membranes in a hot wall tubular CVD reactor using ATI/N_2/O_2 mixtures between 350 and 400 °C and found a linear temperature dependence of the deposition rate.

The discrepancy of literature results shows that the involved chemical mechanisms strongly depend on the geometry of the reactor, in particular on its surface on volume ratio and on the adopted operating conditions, especially on the deposition temperature and on the partial pressure of ATI. More largely, this bibliographic survey reveals that the low pressure MOCVD process for the deposition of alumina from ATI in the temperature range 350-500°C has only been fragmentarily investigated. To the best of the authors' knowledge, no local kinetic modeling of this CVD process was available before our work published in 2011[16] summarized below.

3. *Kinetic model development and validation*

Based on the literature analysis summarized in the previous section, the following apparent chemical heterogeneous reaction was considered:

$[Al(OC_3H_7)_3]_{4(g)} \rightarrow 2\ Al_2O_{3(s)} + 12\ C_3H_{6(g)} + 6\ H_2O_{(g)}$ (R4)

This reaction represents the complete set of unknown homogeneous and heterogeneous chemical reactions involved. Hofman et al.[23] showed that the alumina deposition rate R_{Di}, from ATI can be represented by the following apparent kinetic law:

$R_{Di} = k_0 \exp(-E_a/RT)\ [ATI]^n$ (1)

where k_0 is a pre-exponential constant, E_a (J/mol) an activation energy, T (K) the temperature and n the apparent reaction order (with R_{Di} in kg/m^2/s).

In order to determine the values of these kinetic parameters for the range of operating conditions of interest, dedicated experiments were performed in a horizontal hot wall tubular CVD reactor heated by a Trans Temp transparent furnace. More information can be found in[16]. As received ATI (Acros Organics) was vaporized using a heated bubbler in which pure nitrogen (Air Products) was sent to carry ATI to the deposition zone. The films were deposited on 15 mm*10 mm or on 8 mm*10 mm silicon substrates. They were weighed before and after the alumina deposition using a Sartorius balance (± 10 µg) to determine the deposition rate of the films. The substrate holder was an horizontal aluminium alloy plate with dimensions 1 mm * 358 mm * 19 mm. Seven substrates were used per run, located between 8 cm and 36 cm from the reactor inlet. Four runs were performed using the same deposition conditions except the bubbler temperature and the deposition duration, as detailed in Table 1. The total pressure was of 658 Pa and the total flow rate of 653 sccm in all runs.

Table 1: Investigated operating conditions.

Run	$T_{bubbler}$ (°C)	Deposition duration (min)	Q_{ATI} (sccm)	ATI molar fraction (10^{-2})	ATI mass fraction (10^{-2})
E_1	100	36	1.54	0.24	1.69
E_2	110	21	3.40	0.52	3.68
E_3	90	60	0.70	0.11	0.77
E_4	80	175	0.31	0.05	0.34

Figure 1 presents the axial evolution of the temperature profile measured along the symmetry axis of the reactor as well as the alumina deposition rates deduced from substrates weight difference after and before deposition. The furnace and reactor characteristics led to a temperature profile presenting an isothermal zone close to 490°C between 0.15 and 0.25 m from the reactor inlet. Figure 1 also reveals a strong influence of the bubbler temperature; i.e. of the concentration of ATI, on the alumina deposition rate: a ten degrees increase of the bubbler temperature results in a high increase of the average deposition rate and in a decrease of the deposit thickness uniformity. This is due to a peak in deposition rate existing at the beginning of the isothermal zone and then to a depletion in ATI.

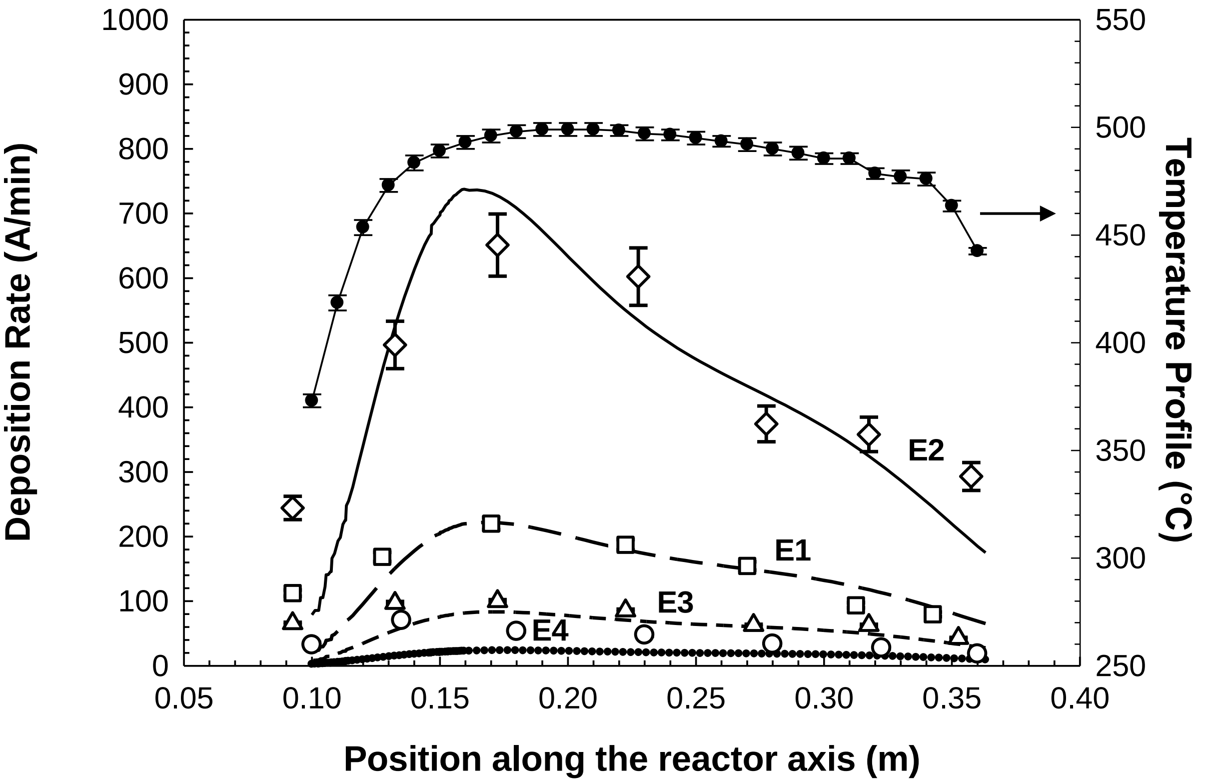

Fig. 1. Experimental axial evolution of the reactor temperature (full circles) and comparison between the experimental (E1: square, E2: diamond, E3: triangle, E4 : circle) and calculated (E1: long dash, E2: solid line, E3: medium dash, E4 : dotted) deposition rates along the reactor axis for runs E1, E2, E3, E4.[16]

Based on the kinetic equation (1), the results of experiments E_1, E_2 and E_3 were used to fit the three parameters k_0, E_a and n. The fitting was performed by virtually dividing the tubular CVD reactor into a series of perfectly mixed cylindrical reactors of 1 cm in length. The deposition rate was assumed to be uniform in each compartment i. An average value deduced from the weighing of each sample was considered for the substrate and for the reactor walls. In these conditions, the following mass balance was written for ATI:

$$Q_{i-1}\, y_{i-1} - Q_i\, y_i = \pm R_{Di}\, S_i \qquad (2)$$

where Q_i (kg.s^{-1}) is the total gas mass flow rate, S_i is the deposition surface and y_i is the mass fraction of ATI in the ith compartment. Q_i was calculated along the CVD reactor by considering the mass of alumina deposited. The inlet mass fraction of ATI at the first compartment was considered equal to that provided by the bubbler at the reactor entrance. By minimizing the error between the experimentally determined deposition rate and the calculated one R_{Di} for the three experiments, the following values of the kinetic parameters k_0, E_a and n were obtained: $k_0 = 1.5\ 10^6$ kg.m$^{2.5}$/(mol$^{1.5}$s), $E_a = 78$ kJ/mol, $n = 1.5$.

This value of E_a corresponds to the main limiting phenomena involved during ATI decomposition and alumina deposition for the conditions tested. As detailed in section 3, Saraie et al.[25] obtained a very close value of 80 kJ/mol by operating between 200 °C and 350

°C at 2000 Pa, with dry N_2 as carrier gas. The apparent order of 1.5 proposed in this work reflects the dependence on ATI concentration of the dominant homogeneous and heterogeneous mechanisms existing in this range of operating conditions. It can be compared with the value of 1 adopted by Kawase et al.[19] between 830 and 1160°C and with the value of 2 found by Hofman et al.[23] at temperatures slightly lower than the present ones.

This kinetic law was implemented into the CFD code Fluent and the results obtained in terms of deposition rate along the reactor axis are compared with the experimental results in Figure 1. The average relative error for the three experiments is of 18 %. This error can be attributed to several factors, including the uncertainty of the inlet flow rate of ATI, due to that of the ATI saturation pressure law and the use of a simplified apparent kinetic law. The model was used to simulate the deposition rate profile for run E4 (not used for the establishment of the kinetic data). The obtained profile together with the experimental deposition rates are also reported in Figure 1. A satisfactory agreement is observed, which validates as a first approach the kinetic model for the investigated range of operating conditions. This is the reason why the model has then been applied to another reactor operating in the same range of deposition conditions, but treating a complex substrate.

4. *Optimization of an original reactor by process simulation*

As detailed elsewhere[17], a direct liquid injection (DLI) MOCVD process was developed to deposit alumina thin films from ATI on the internal surface of glass vials. The term “DLI-MOCVD” refers to reactors, which use liquid delivery units to feed the deposition zone in reactants.[27] This technology allows performing reliable, accurate and repeatable vaporization of liquid and dissolved solid compounds and precursors since it is much easier to regulate precisely a liquid flow rate than that of powders. The aim was to form an anti-corrosion barrier against aggressive liquids which could be stored into the vials. The uniform deposition of thin films inside the inner surface of a closed geometry is a non-trivial target since the complex gas flow strongly interacts with the species local concentration profiles and then with the local deposition rates. Developing such a process from scratch purely empirically would have been time and cost consuming. We then decided to combine coating experiments and process simulation to develop and optimize the process.

The DLI-MOCVD reactor is schematically represented in Figure 2. The glass vial to coat (4.25 cm in diameter, 7.3 cm in height) is put on a substrate holder in an inductively heated vertical quartz tube (5.5 cm in diameter, 33.5 cm in height).

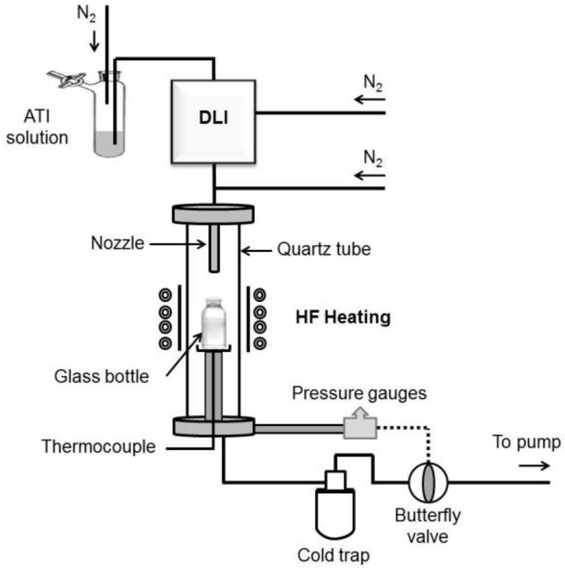

Figure 2: Schematic of the DLI-MOCVD reactor for the Al_2O_3 deposition inside a vial.[17]

All experiments were performed at a temperature of 480°C on the external surface of the central part of the vial bottom. Figure 3 shows the experimentally measured thermal profiles on the inner walls of the vial for various reactor configurations, as it will be detailed below. ATI was dissolved in cyclohexane and then the solution was atomized and vaporized in a Kemstream Vapbox 500® DLI instrument. This reactive gas phase was diluted with pure N_2 and introduced into the reactor through a SS nozzle. The total gas flow rate was of 585 sccm and the inlet ATI molar fraction was fixed at 1.7 10^{-3}. The total pressure was of 666 Pa, close to the value used in the tubular reactor.

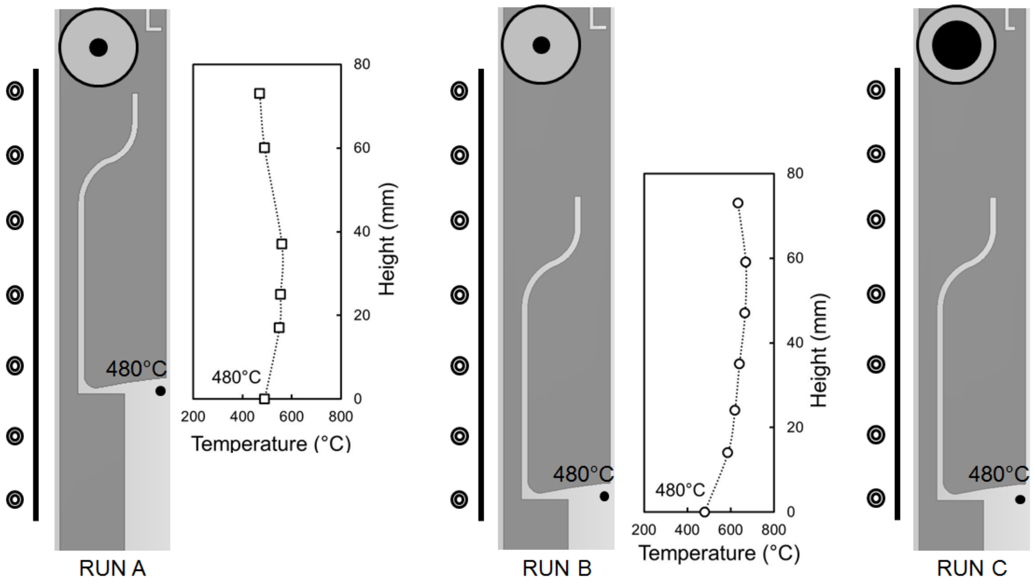

Figure 3: Schematic representation of the reactor for runs A, B and C with relative positions of the bottle, the heating tube and the nozzle, associated with the experimental thermal profiles. The circles on the top represent bottom views of the nozzle outlet with the feeding hole in black.[17]

After deposition, the deposit thickness profile was measured by scanning electron microscopy (SEM) on a LEO 435VP instrument after fracture of the vials.

A first set of runs called Run A was performed with an arbitrary fixed distance between the nozzle and the vial of 15 mm and with a 2 mm inner nozzle diameter at its outlet. The experimental thickness profile along the internal walls of the vial is presented in Figure 4a. The thickness on the lateral walls (height of bottle from 20 to 55 mm) ranged between 600 and 1,000 nm. An over-thickness was observed at the lower part (up to 5,600 nm from 0 to 20 mm) and at the entrance (up to 1,300 nm from 55 to 70 mm). Visually, the thickest zone appeared as a powdery white layer while the other parts remained optically transparent. Cross-section SEM analyses of the deposit (not shown) revealed that that the powdery zone was composed of spherical particles aggregated on the film surface, whereas the other zones were dense and smooth. The simulated thickness profile using the kinetic law developed in the previous section is shown in Figure 4a. A good agreement can be observed between the experiment and the model only in the regions where the deposit is smooth and dense. This can be explained by the fact that a different deposition mechanism probably exists for the powdery zone, which is not represented by the model.

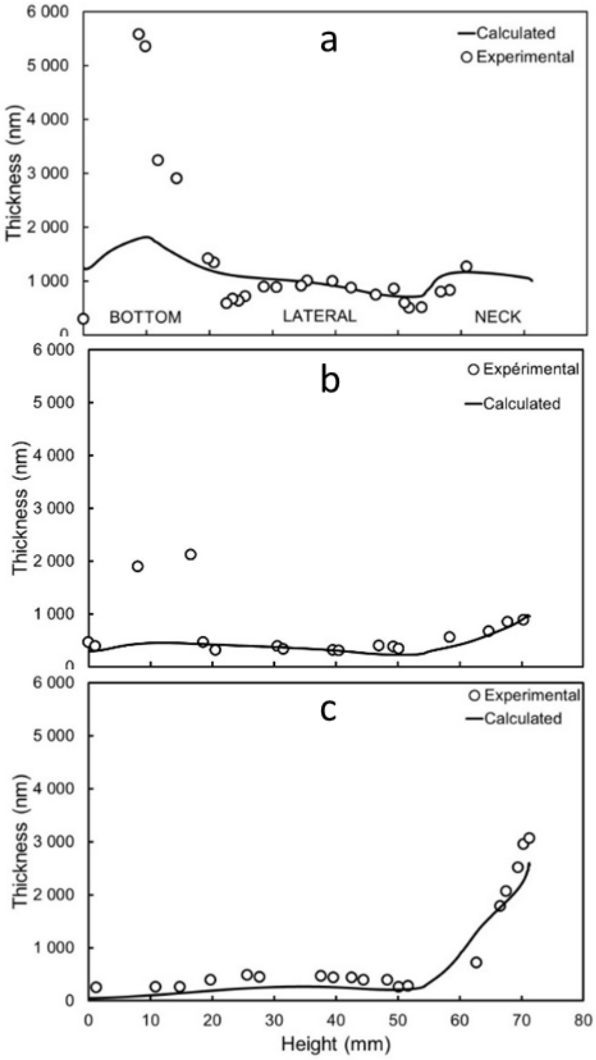

Figure 4: Comparison between the experimental and the calculated thickness along the vial height for (a) run A, (b) run B, (c) run C. Adapted from [17].

In order to better understand the mechanisms involved, the local gas velocity profiles are plotted in Figure 5 RUN A into the reactor and at the bottom of the vial in Figure 6 RUN A. The scales of velocities respectively higher than 100 and 150 m/s are saturated for a better representation of the flow. At the nozzle outlet, the gas velocity is very high (470 m/s) due to its narrow section. This creates an impinging jet perpendicular to the vial bottom surface with high gradients and a sharp change of direction after hitting the bottom surface. When zooming at the bottom corner (Figure 6 RUN A), a recirculation loop is present. The high residence time of the gas in this loop could explain the formation of the white powdery deposit by gas phase nucleation. Figure 7 presents the ATI molar fraction into the reactor. The ATI concentration is not uniform into the vial and especially near its inner walls. The zones of highest ATI concentration correspond logically to the regions with the thickest deposits (neck and bottom).

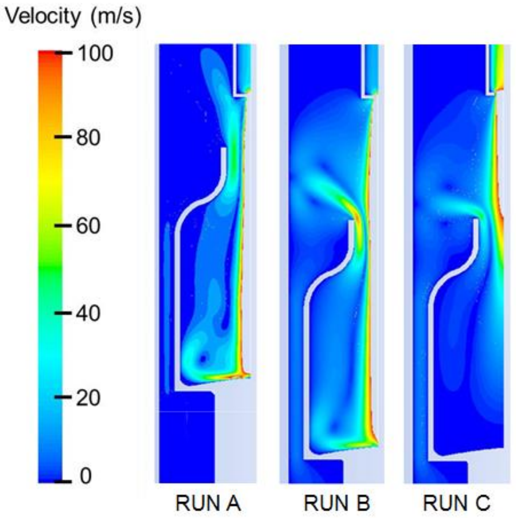

Figure 5: Simulated profiles of the local gas velocity in the reactor for the three runs.[17]

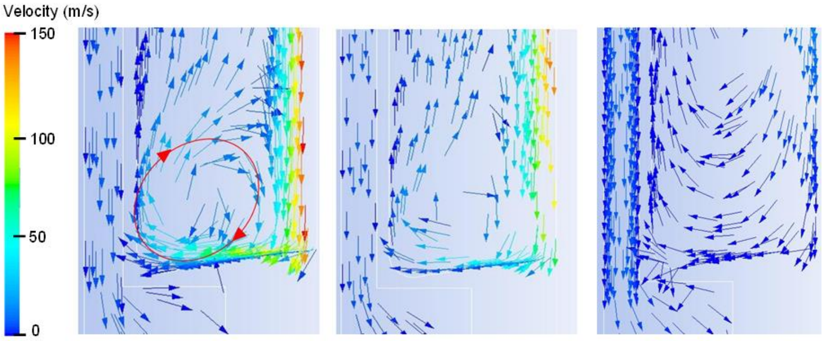

Figure 6: Simulated profiles of the local gas velocity for the three runs at the bottom of the vial.[17]

New simulations were then performed aiming to decrease the velocity of the impinging jet in order (i) to limit the recirculation zone leading to the powdery deposit and (ii) to have more uniform ATI local concentrations near the inner walls of the vial, so more uniform deposit thicknesses. After several trials, this was achieved (Run B) by increasing the distance between the nozzle and the vial from 15 mm to 40 mm. Experimentally, the setup was modified accordingly and the vial was then translated toward the bottom part of the heating system, leading to a new measured thermal profile (Figure 3b). The corresponding local gas velocity profiles calculated into the reactor and at the bottom of the vial are detailed in Figures 5 RUN B and 6 RUN B respectively. The phenomena of impinging jet and of recirculation still exist but are attenuated. Figure 7 RUN B shows that the local ATI molar fraction profile is more uniform near the vial walls. However, the corresponding experimental results indicated that a white powdery thicker deposit was still present in the bottom corner of the vial, this over-thickness can be seen in Figure 4b. A transparent dense layer coated all the other parts of the vial. The thickness at the neck and on the lateral walls of the vial was uniform while a slight over thickness was present at the vial entrance. The model reproduces well this behavior, except another time the powdery high thickness zone.

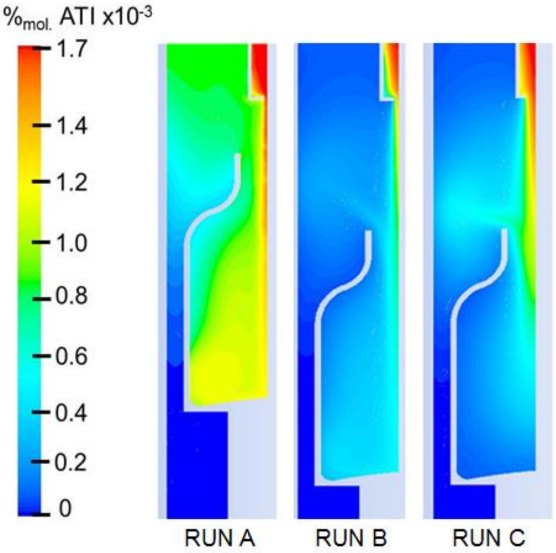

Figure 7: Simulated profiles of the local ATI molar fraction in the reactor for the three runs.[17]

New simulations were performed in order to still decrease the velocity of the impinging jet. As the total gas flow rate was imposed by the DLI system, the simplest way found was to increase the inlet diameter of the nozzle outlet from 2 mm to 5 mm, keeping the distance between the nozzle and the vial fixed at 40 mm. This new reactor configuration called Run C can be seen in Figure 3. Figure 5 RUN C indicates that the velocity profile inside the vial is different from Runs A and B. An impinging jet is no more present inside the vial, even if the inlet flow is mainly axial. The gas velocities are also much lower, not exceeding 100 m/s. Consequently, Figure 6 RUN C shows that the gas flow reaches the bottom part of the vial smoothly and no recirculation loop is present. The ATI concentration profile inside the vial (Figure 7 RUN C) is more uniform near the inner walls, but the convective transport being decreased, the local ATI concentrations are lower. The corresponding calculated thickness profile is presented in Figure 4c. From 0 to 55 mm, the thickness is quite uniform, ranging from 250 to 450 nm and is logically lower than for Runs A and B. An over-thickness is present on the neck walls till 3,000 nm due to the higher ATI concentration existing in this zone. The calculated profile is in good agreement with the corresponding experimental thickness profile.

II. Local coordination affects properties: The case of amorphous Al_2O_3 barrier coatings.

Following Aboaf's pioneering works [28], ATI is one of the most commonly used, single source precursors for the deposition of alumina films. It presents significant advantages since it is stable in air, only slowly reactive with water, and it is cheap. Once melt, it remains liquid below the melting temperature, its vapors can thus be transported to the process chamber by simply bubbling through a carrier gas. MOCVD of Al_2O_3 from ATI at moderate deposition temperature (T_d) was first used to coat thermally sensitive semiconductor materials with isolating films in transistor devices. Films of Al_2O_3 were deposited in the range 350 – 500 °C.[28-34] The intrinsic corrosion resistance[35], and the use of such films for the protection against corrosion of stainless steel[7] and of titanium alloys[36] were investigated. Most of these works were more pragmatic approaches to tune film properties rather than systematic investigations on the correlation between experimental parameters and film composition and properties. Compositional uncertainties are frequently reported for the films prepared at the lowest T_d. More fundamental approaches were tentatively carried out with films grown in hot-wall reactors, by Morssinkhof [37-39], by Yoshikawa et al.[40] and by Vahlas et al.[16, 41, 42]

However, ATI does not meet all the criteria required for an ideal MOCVD precursor. Its shelf-life, polymerization, and the condensation behavior of its tetramer during thermal ageing are problematic[42] and lead to worsening film properties as well as to tedious reactor maintenance due to line pollution and injector blockage. Besides ATI, other volatile aluminium compounds have been proposed: aluminium tri-(2-ethylhexanoate),[43] aluminium tri-(*sec*-butoxide),[44-46] aluminium (ethylacetoacetate)-di-isopropoxide,[26] aluminium triacetylacetonate,[47-49] dimethyl, diethyl and di-*iso*-butyl aluminium acetylacetonate,[50] and dimethyl aluminium isopropoxide (DMAI). [10, 11, 51-53, 54, 55, 56, 57] The latter consists of an Al atom linked to two methyl and one isopropyl groups, and has an intermediate structure between ATI and trimethyl aluminum (TMA). Unlike TMA, the remaining isopropyl group in DMAI stabilizes the molecule, which is non-pyrophoric. Moreover, the molecule presents a significantly higher vapor pressure than ATI, it is liquid at room temperature, has a longer shelf life and is not prone to polymerization. The use of ATI and DMAI for the CVD of alumina will be taken as example of the impact of the precursor chemistry on the characteristics and the properties of the obtained films.

The generation of precursor vapors and their transport to the process chamber through the sublimation and the vaporization of solid and liquid precursors, respectively, presents *a priori* simplicity and cost effectiveness. Nevertheless, maintaining of temperature sensitive precursors such as ATI at the vaporization temperature for a long period impacts the stability of the molecule and subsequently the coating quality.[42] In addition, it is difficult to access and control the generated reactive gas mass flow rate. This poorly controlled situation leads to non-reproducible operation, especially in cases where low activation energy prevails in the entire temperature range of interest, resulting in mass transport limited process. The direct liquid injection (DLI) technology allows overcoming these drawbacks with the controlled atomization and vaporization of pure liquid precursors or of solid ones dissolved in an appropriate carrier solvent.[58-61] Both vaporization and DLI technologies will be used hereafter to feed the process chamber with the alumina precursors.

1. *Microstructure of amorphous alumina films*

Figure 8 presents cross-sectional SEM images of Al_2O_3 CVD films, deposited on Si wafers at 5 Torr from ATI (left column) and from DMAI (in the presence of O_2, right), with the precursor molecules shown on top. The films are processed either by vaporization of the precursor (up, from ATI only) or from DLI (lower row), with the schematic of a bubbler and the photograph of a DLI equipment shown on the left of the upper and lower rows, respectively. Process temperature is indicated in each case. The AFM 3D topography image of the surface of the film processed from DMAI is also presented. Its scale spans from 0 to 15 nm. Films diffract neither X-rays nor electrons, with a characteristic electron diffraction pattern shown in the center of the figure. They are dense and present pinholes-free, highly smooth surfaces, witnessed by low roughness values, such as 1.35 nm and 1.71 nm for the arithmetic and rms, respectively, of the DLI DMAI/O_2 sample. The only exception concerns the film processed from ATI by DLI, which is still smooth but slightly porous with nanometer cavities over the entire height. This particular morphology is attributed to the presence of the solvent, in this case cyclohexane in the DLI process.

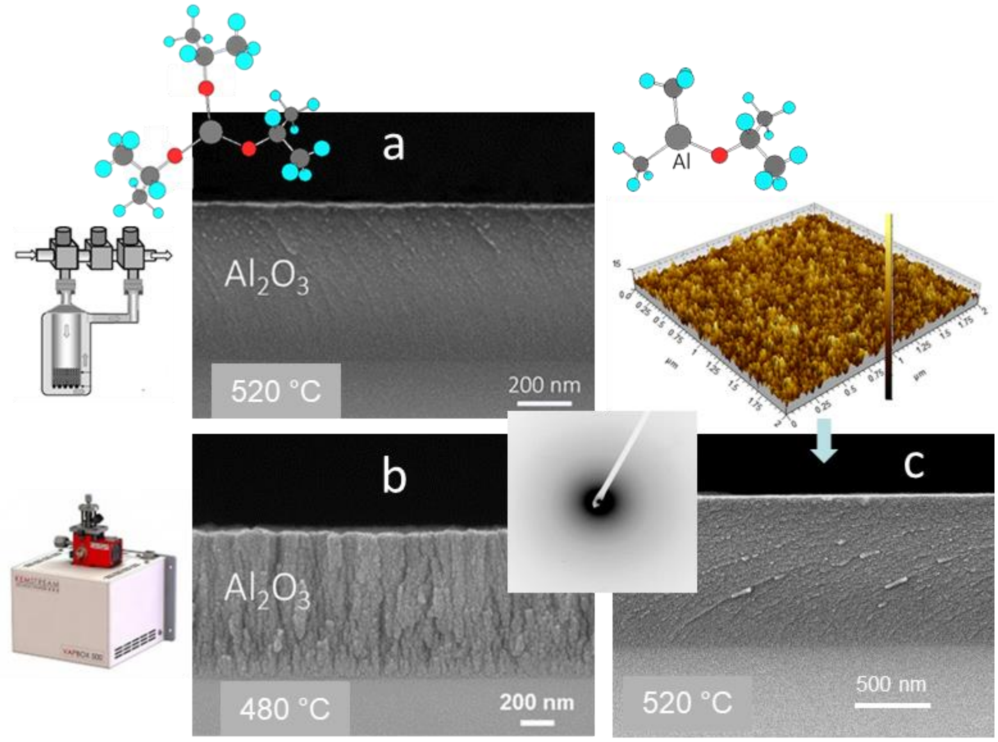

Figure 8. Cross-sectional SEM micrographs of Al_2O_3 CVD films deposited on Si wafers from ATI (a, b, left column) and from DMAI (c, right column), with the precursor molecules shown on top. The films are processed either by sublimation of the precursor (upper row) or from DLI (lower row). Temperatures refer to process conditions. The atomic force microscopy (AFM) 3D topography image is that of the surface of the film processed from DMAI with a

vertical scale spanning from 0 to 15 nm. The electron diffraction pattern shown in the center of the figure is characteristic of all samples. Adapted from [62],[63].

The O/Al ratio of such films was determined by electron probe for microanalysis (EMPA) using internal standards. It is presented in Figure 2 as a function of T_d and is compared to the ratios expected for AlOOH and Al_2O_3 references. Their carbon content was determined by X-ray photoelectron spectroscopy (XPS).

Films deposited from both evaporated and DLI ATI present O/Al ratios of 2.12 and *ca.* 1.7 when deposited at 360 °C and 420 °C, respectively. These values correspond to compositions close to AlOOH (atomic ratio 2.0) and partially hydroxylated $AlO_{1+x}(OH)_{1-2x}$ films. Films deposited between 470 °C and 650 °C show O/Al ratios close to, though slightly higher than 1.5, in good agreement with the formula Al_2O_3. The presence of hydroxylated aluminas at low T_d and the decrease of the concentration of hydroxyl groups with increasing T_d is confirmed by the O1s binding energy shown in the lower part of Figure 9. At higher T_d (700 °C), the O/Al ratio decreases to 1.44. The C content is below 1 at.% for all T_d below 650 °C, while a small concentration of ca. 4 at.% C is detected by XPS. The XPS probed C1s binding energy reveals that this carbon is almost exclusively related to aliphatic moieties, and most likely results from carbon residues of ATI isopropoxide ligands trapped in the film.

The films deposited from DMAI at 150 and 200 °C in the presence of H_2O vapor show O/Al atomic ratios of 1.81 and 1.67, respectively. These values are contained between those of AlOOH and Al_2O_3 (1.5), thus revealing partially hydroxylated alumina $AlO_{1+x}(OH)_{1-2x}$. The O/Al ratio of films prepared at 250 °C and above is in good agreement with the formula Al_2O_3. This result is confirmed by the evolution of the O1s binding energy which, above this T_d reveals the presence of O-Al bonds, exclusively. It is concluded that stoichiometric alumina films can be processed in this way for the protection and surface functionalization of thermally sensitive parts. The C content of such films is below 1 at%. The film prepared at 500 °C in the presence of O_2 has an O/Al ratio of 1.48, which may be ascribed to the formula Al_2O_3. The films prepared at 600 and 700 °C have O/Al ratios of 1.25 and 1.10, well below 1.50. The decrease in O/Al ratio is clearly related to an increase in the C concentration, up to about 6.5 at% in the film prepared at 700 °C, as has been also evidenced by Schmidt et al. during the preparation of alumina films from sublimed DMAI in this T_d range.[56, 64] This suggests the formation of the aluminum carbide Al_4C_3 and/or of aluminum oxycarbides, e.g. Al_4O_4C or Al_2OC [40, 41, 42, 43], along with Al_2O_3, to lead to the generic composition of $Al_2O_xC_{3/2-x/2}$. The formation of oxycarbides can be thought to result from the partial substitution of one C^{4-} anion for two O^{2-} anions, leading to the formulas Al_4O_4C, Al_2OC, and ultimately Al_4C_3, as also illustrated by the strong C-Al bond contribution in the C1s binding energies at 600 °C and above.[63]

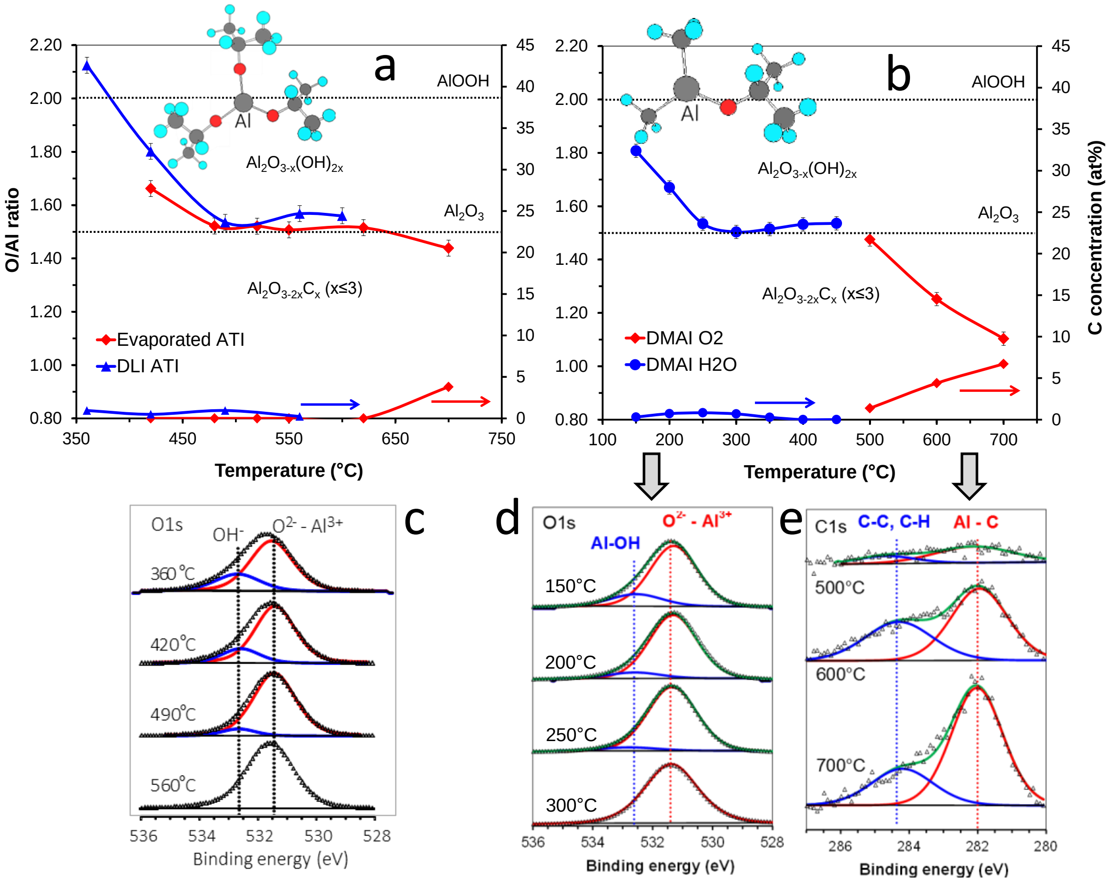

Figure 9. Top: O/Al atomic ratio and C content of the alumina films prepared from evaporated ATI and from DLI CVD of ATI (a), and from DLI CVD of DMAI in the presence of H_2O and of O_2 (b). For both diagrams the left ordinate corresponds to the O/Al ratio and the right one to the C-concentration (at%). Bottom: High resolution X-ray photoelectron O1s et C1s spectra of alumina films deposited from ATI in the range 360 °C – 560 °C (c), from DMAI + H_2O in the range 150 °C – 450 °C (d) and from DMAI + O_2 in the range 500 °C – 700 °C (e). Adapted from [57],[62].

The above resumed compositional and property variations of the alumina films are indicative of modifications of the amorphous structure upon changing T_d. We showed that for the films of general formula $AlO_{1+x}(OH)_{1-2x}$, structural modifications are expected to accompany dehydroxylation from AlOOH to Al_2O_3 with increasing the T_d up to 250 °C for the DMAI process and up to 450 °C for the ATI one. $\{^1H\}^{27}Al$ rotational echo double resonance (REDOR) nuclear magnetic resonance (NMR) experiments performed on films obtained from vaporized ATI confirm this trend.[65] The question arises as to possible further structural modifications in Al_2O_3 for the films grown at higher T_d. This question is investigated for both systems by very high-field (20 T) ^{27}Al NMR and the main results are resumed in the next paragraphs.

The left part of Figure 10 illustrates the 2D ^{27}Al 3-quantum magic-angle spinning nuclear magnetic resonance (3QMAS NMR) spectra of alumina films processed from vaporized ATI at six different T_d.[65] The use of very high magnetic field allows high spectral resolution and yields a clear identification of the tetra-, penta-, and hexa-coordinated aluminum sites ($^{[n]}Al$ with n =

4, 5, or 6). Their line shapes are characteristic of a typical amorphous structure as seen in alumina-containing glasses. The percentage of each $^{[n]}$Al site was calculated from these and from the corresponding 1D ^{27}Al MAS spectra. Its evolution with T_d is drown in the upper left part of the figure. The respective percentages of tetra- and hexa-coordinated sites vary with opposite trends. The $^{[4]}$Al content increases from 33 % for T_d = 360 °C up to 53 % for Td = 480 °C; at the same time, the $^{[6]}$Al content decreases from 26 % to 5 %. For T_d = 550 °C, the respective percentages have values that are nearly the same as those for 480 °C, suggesting that the maximum of $^{[4]}$Al sites and the minimum of $^{[6]}$Al sites occur at ∼515 °C. From 360 to 515 °C, the $^{[5]}$Al content is at its highest with values between 40 % and 43 %. It can be noticed that the $^{[n]}$Al percentages measured for T_d = 480 °C (and 550 °C) compare well with those measured by Lee et al. for two aluminum oxide films prepared by PVD and ALD.[66, 67] In the 550−720 °C range, the $^{[6]}$Al content increases to 59 % and the $^{[4]}$Al and $^{[5]}$Al contents decrease to 29 % and 12 %, respectively. The lower right diagram of Figure 3 shows the evolution of chemical shift distribution (ΔCS) of each $^{[n]}$Al environment. ΔCS is maximal for a T_d more or less half-way between 480 and 550 °C for each coordination number. This suggests that the utmost structural disorder corresponds to the highest rates of $^{[4]}$Al and $^{[5]}$Al sites.

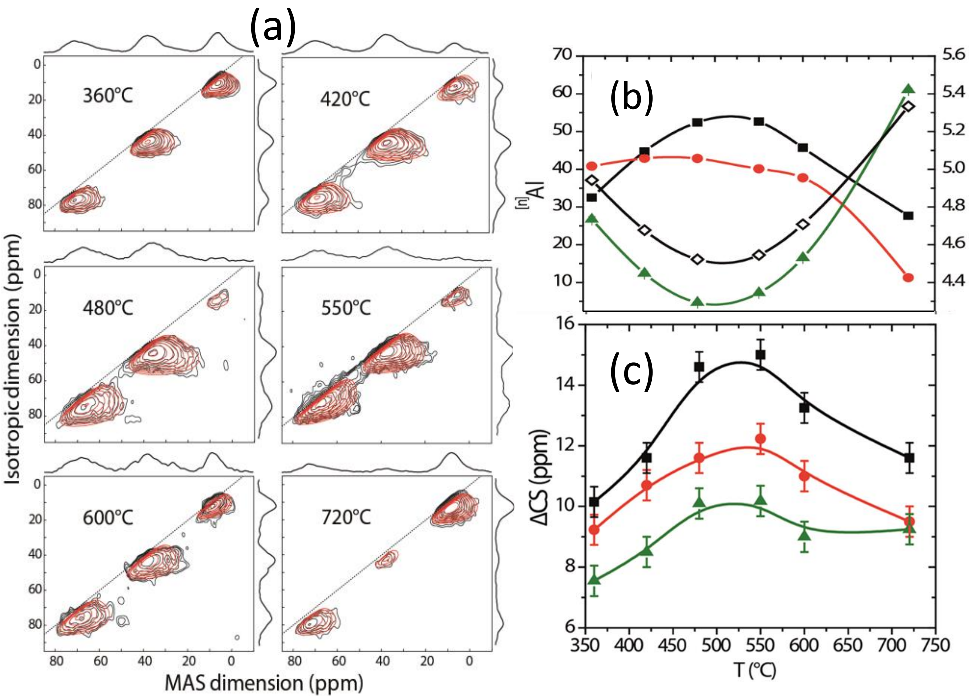

Figure 10. (a): Two-dimensional ^{27}Al 3QMAS spectra of the films deposited at different temperatures. Black and red lines refer to experimental and simulated spectra, respectively. (b): Percentages of the $^{[n]}$Al environments and (c): their corresponding chemical shift distributions (ΔCS), as a function of T_d. Black squares, red circles, and green triangles refer to $^{[4]}$Al, $^{[5]}$Al, and $^{[6]}$Al sites, respectively. Open diamonds in (b) correspond to the averaged coordination number calculated from the formula CN = [4 ($^{[4]}$Al atom %) + 5 ($^{[5]}$Al atom %) + 6 ($^{[6]}$Al atom %)]/100. All lines are a guide to the eye. Adapted from [65].

A similar, nuclear magnetic-resonance spectroscopy (NMR) investigation was applied to the films processed from DMAI.[68] As an example, the left part of Figure 11 presents 1D ^{27}Al MAS NMR spectra of alumina films prepared from DMAI + O_2. All spectra consist of 3 or 4 overlapping broad lines each corresponding to a specific Al coordination, characteristic of amorphous alumina-containing materials. The spectral reconstructions evidence $^{[4]}$Al (AlO_4), $^{[5]}$Al (AlO_5) and $^{[6]}$Al (AlO_6) coordination units in all films. Furthermore, an additional broad line centered at around 90 ppm is detected for the films processed at 600 °C and 700 °C, which suggests the presence of a carbon containing aluminum environment. The reported in the figure 2D 3QMAS spectrum for the 700 °C sample confirms the presence in the film of these four Al environments. The diagram on the right of Figure 11 presents the distribution, as a function of T_d, of the concentrations (at%) of the four Al environments in films processed from DMAI plus H_2O (up to 300 °C) and from DMAI plus O_2 (from 500 °C and above). The $^{[4]}$Al and $^{[5]}$Al concentrations increase(decrease) with increasing T_d for films processed in the presence of H_2O(O_2). All corresponding $^{[n]}$Al values evolve in a way which allows assuming either a saturation or a maximum of $^{[4]}$Al plus $^{[5]}$Al coordination environments in the T_d range 300 – 500 °C. In this T_d range the concentration of the $^{[6]}$Al coordination environments reaches a remarkably low value of less than 5 at%. The carbon containing aluminum environment is null at T_d less or equal 500 °C; it strongly increases at higher T_d and approaches 30 at% at 700 °C.

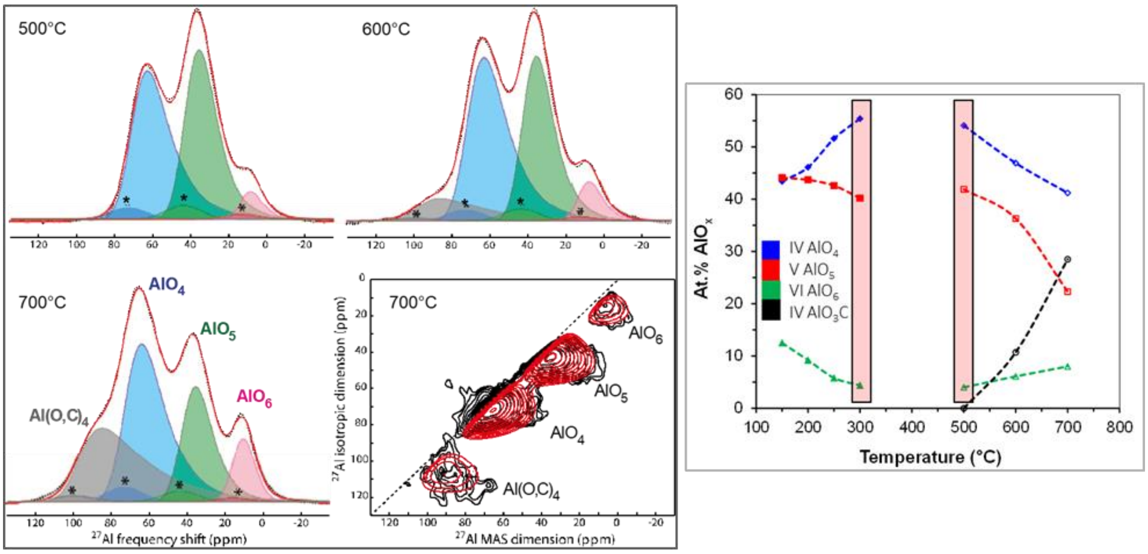

Figure 11. Left: Experimental (dashed black lines) and reconstructed (full red lines) ^{27}Al MAS NMR spectra of alumina films prepared from DMAI plus O_2 from 500 to 700 °C. The 2D 3QMAS for 700 °C is shown as an example. The AlO_4 (blue), AlO_5 (green), AlO_6 (pink) and $Al(O,C)_4$ (grey) coordination environments are fitted with their respective MAS-related sidebands (*) which correspond to the bands n = 0 of the external transitions. Right: Distribution, as a function of T_d, of the AlO_4 (blue diamonds), AlO_5 (red squares), AlO_6 (green triangles), and $Al(O,C)_4$ (black circles) concentrations (at%) in films processed from DMAI plus H_2O (full symbols) and from DMAI plus O_2 (open symbols). Pink bars reveal investigated process temperatures resulting in films with maximum AlO_4 plus AlO_5 coordination environments. Adapted from [68].

The impact of the distribution of the [n]Al environments of films processed from vaporized ATI on different properties of such films is presented in Figure 12. The bottom diagram of the figure resumes the compositional and structural information of the films and their evolution as a function of T_d. The middle diagram presents the corresponding evolution of their hardness and of the Young modulus, determined from nanoindentation experiments on alumina films deposited on Ti_6Al_4V titanium alloy.[12] The hardness increases with increasing T_d up to 480 °C, where it reaches a maximum value of 10.8 ± 0.8 GPa. Similar trends are obtained for the modulus, which increases from 92 ± 8 GPa to 155 ± 6 GPa with increasing T_d from 350 °C to 480 °C. The value of both parameters vanishes at T_d 750 °C, because at this temperature, the film becomes nano-crystallized and thus it presents limited cohesion and high roughness. The upper diagram presents the evolution, with increasing T_d of the impedance modulus, obtained after 1 h of immersion in a 0.1 NaCl solution, for films deposited on Ti6242 titanium alloy.[36] The film deposited at 480 °C stands out by improving the corrosion resistance of nearly two orders of magnitude in comparison with the uncoated sample, whose impedance modulus is 1.3×10^5 Ω cm^2). Contrastingly, films processed at 350 °C and at 750 °C slightly improve the corrosion resistance of the bare alloy. The evolution of the contact angle with pure water is also presented in this diagram.[69] It slightly increases from 103±1 ° at 350 °C to 106 ± 2 ° at 480 °C, these values illustrating the hydrophobic nature of the amorphous aluminum oxyhydroxides and alumina surfaces. It decreases to 48±3 °at 700 °C, revealing the hydrophilic nature of the surface of the nanocrystalline film.

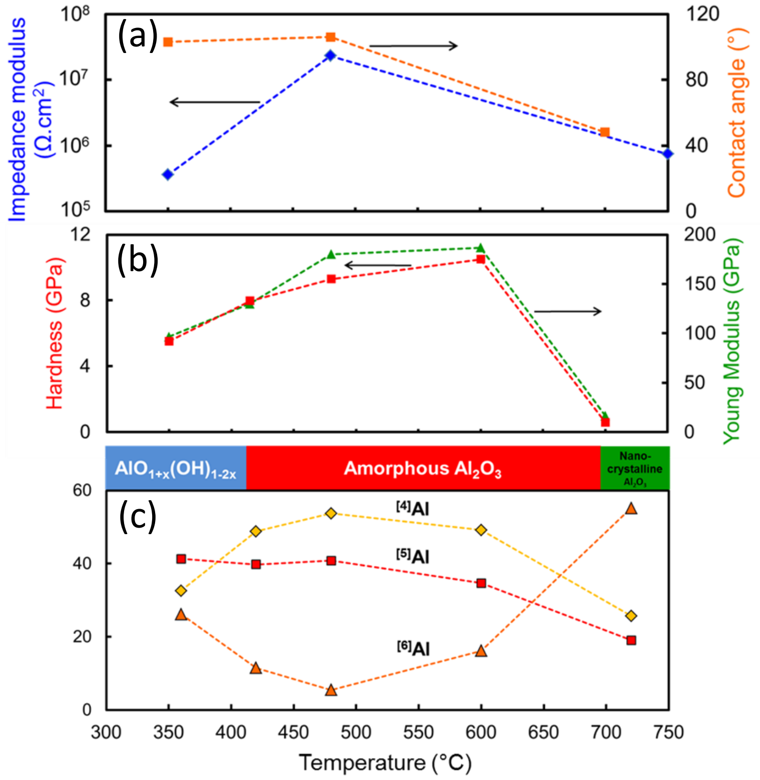

Figure 12. Evolution of the impedance modulus and the contact angle with water (a), of the hardness and the Young modulus (b) as a function of deposition temperature for alumina films processed from evaporated ATI. (c): Corresponding evolution of the concentration of

the [4]Al, [5]Al, and [6]Al sites and of the composition and the crystallinity of the films. Adapted from [12],[70],[69].

2. *Application examples of barrier function of amorphous alumina films*

Such alumina films find applications in a large number of key enabling technologies. Two examples will be sketched hereafter to illustrate this utility.

The first concerns the protection of lightweight titanium alloys against high temperature oxidation. We have already provided selected data from this research in the previous paragraphs to illustrate intrinsic characteristics of the alumina films. Here, we focus on their capacity to durably protect such alloys in operating conditions, which simulate the operation of specific parts of aero turbines. The scope of the work is to extend the implementation of Ti alloys to hotter parts of the turbine, in replacement of stainless steel. The limited resistance of these alloys to high temperature oxidation hinders this implementation. It is due to the rapid formation on the surface of titanium alloys in contact with the air, of a very stable, non-protective titanium oxide layer, and also, to the ingress of oxygen at interstitial position in the alpha phase of these alloys.[71, 72]

Alumina films were deposited on all faces of a near-alpha titanium alloy coupons Ti6242S from both ATI and DMAI following the previously described CVD processes. Figure 13 presents parabolic rate constants k_p for the oxidation of the Ti6242S alloy, bare and coated with ca. 500 nm thick amorphous alumina processed from DMAI at 300 °C (DMAI300) and at 500 °C (DMAI500), and from vaporized ATI at 520 °C (ATI520). The values were calculated according to the equation: $k_p = [(\Delta m_f/S)^2 - (\Delta m_i/S)^2]/(t_f - t_i)$, where Δm_i and Δm_f are respectively the mass gain of a sample with free surface S, at the beginning, t_i and at the end, t_f of each temperature dwell. The diagram shows that the three coatings DMAI500, DMAI300 and ATI520 (where the codes correspond to alumina deposition from DMAI at 550 °C and at 300 °C, and from vaporized ATI at 520 °C, respectively), are efficient for oxidation protection during the short term (10 to 20 h) thermogravimetric experiment, between 600°C and 700°C. They are less efficient at 800°C except for the DMAI500 one, and they are inefficient at 900°C. This first set of TGA experiments was completed by long term oxidation annealing in laboratory air at 600 °C, which is close to the maximum temperature of use of such alloys. The weight gain of the DMAI500 coated coupon after 5000 h is ca. 0.20 $mg*cm^{-2}$, to be compared with 1.63 $mg*cm^{-2}$ for the bare alloy. The surface micrographs of the two samples are presented in the bottom right side of Figure 13. The whole surface of the bare alloy is covered with thin, few-micrometers-long needles. This morphology corresponds to the well-known acicular rutile that forms when Ti6242S is exposed to oxidation treatments.[73] The surface of the DMAI500 coated coupon presents a smaller number and thinner needles than those observed on the oxidized Ti6242S. The formation of a few excrescences on the surface, one of which is shown in the left bottom part is due to scarce defects of the coating, probably created from homogeneous nucleation during deposition. These results confirm the excellent oxidation protection conferred to Ti6242S by the 500 nm thick amorphous Al_2O_3 films.

Figure 14 shows SEM images in backscattered electrons mode of cross-sections obtained by focused ion beam (FIB), and corresponding electron dispersive spectroscopy (EDS) maps of a bare Ti6242S alloy (micrographs a-d) and a coated coupon (e-h) after oxidation at 600 °C during 5000 h. The bare Ti6242S cross-section after oxidation (a) can be divided into 3 layers. The top 1.6 µm-thick layer corresponds to the needles observed on the surface, with a great density of large open pores. The intermediate layer is 2 µm-thick, with a high density of small pores. The deepest region corresponds to the bulk part of the sample with the known microstructure of the alloy. The EDS mapping (b-d) reveals that a (Al, Ti) mixed oxide is formed on the top layer of the acicular rutile TiO_2 with a clear preferential segregation of Al from the bulk to the free surface. In contrast, the intermediate layer mainly contains Ti and O. After oxidation of the coated coupon, its microstructure and chemical composition are strongly modified. The cross sectional SEM micrograph (e) shows the presence of pores in the vicinity of the initial alumina/Ti6242S interface. In this porous region, the Al_2O_3 coating has been replaced by a mixed Ti, O, Al layer. The thickness of the initial alumina protective film has been reduced by half at the end of the oxidation. Finally, the behavior of the coated coupons was also evaluated under thermal cycling conditions. Indeed, in such conditions spallation of the ceramic coating on the metallic substrate may rapidly occur resulting in limited durability of the material. The tests are performed with a TGA apparatus which allows thermal cycling with continuous recording of the mass.[74] The sensitivity on mass variation of the instrument is 0.1 µg, allowing for detection of tiny spallation events. 80 one hour cycles were performed between 50 °C and 600 °C, under flowing synthetic air. The top right insert of Figure 13 presents the evolution of the mass gain per unit area of the DMAI300 coated sample, and of the temperature variation as a function of time. No mass gain or mass loss could be detected for this sample at the microgram scale. Despite the fact that this test is rather short compared with the usual service periods in turbine applications, it is still a valuable indicator of the excellent adherence of the alumina layer and of the relatively low level of elastic strain energy in the system during thermal cycling. These results confirm the efficiency of the protection of the alloy by the alumina coating. The considered CVD processes are transferable and can be used for the surface treatment of parts of aeroturbines with complex shapes.

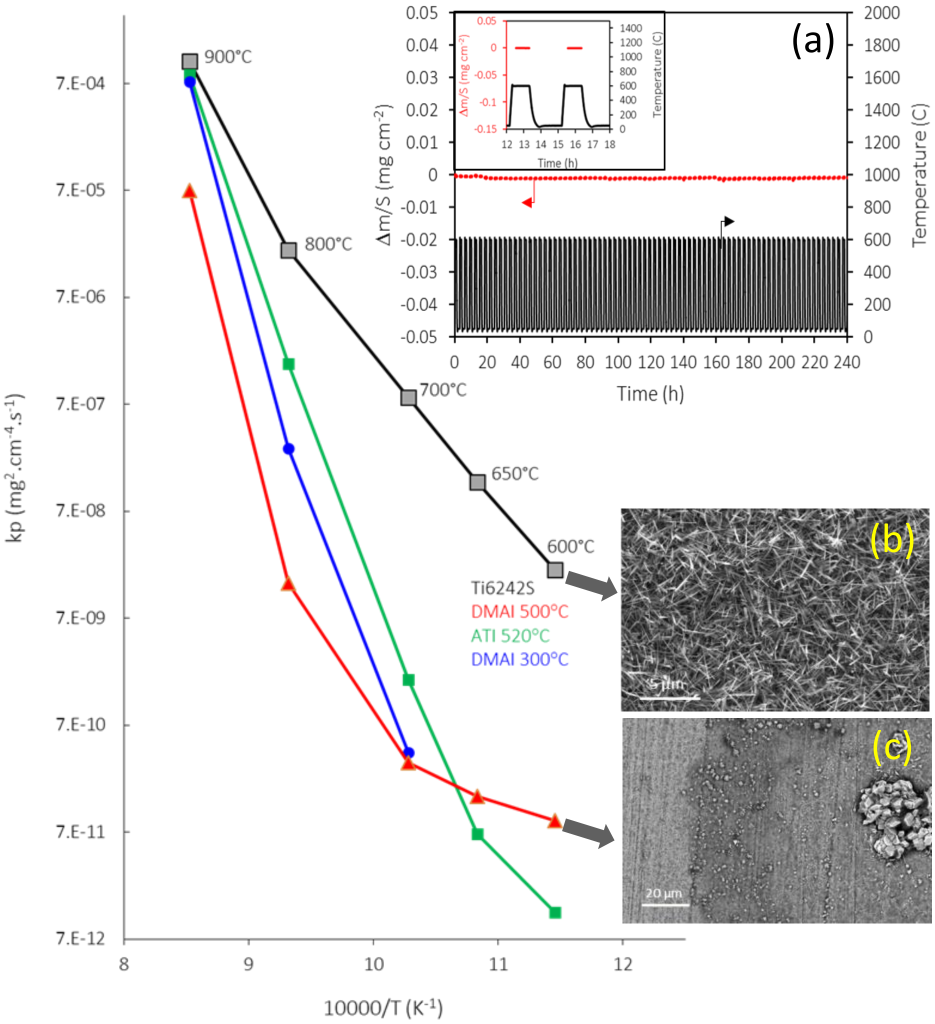

Figure 13. Parabolic rate constants for the oxidation of the Ti6242S alloy, bare and coated with amorphous alumina processed from DMAI at 300 °C (DMAI300) and at 500 °C (DMAI500), and from vaporized ATI at 520 °C (ATI520). Results are compared with the kinetics of the development of gamma, theta and alpha alumina on NiAl, from [75]. (a): Evolution of the mass gain per unit area of the DMAI300 sample, and of the temperature variation (cycling) as a function of time. The insert is a zoom on two cycles, detailing the temperature profile. (b) and (c): Surface SEM micrographs of two samples after 5000 h of isothermal oxidation at 600°C: bare Ti6242S (b), and DMAI500 coated coupon (c). Adapted from [76].

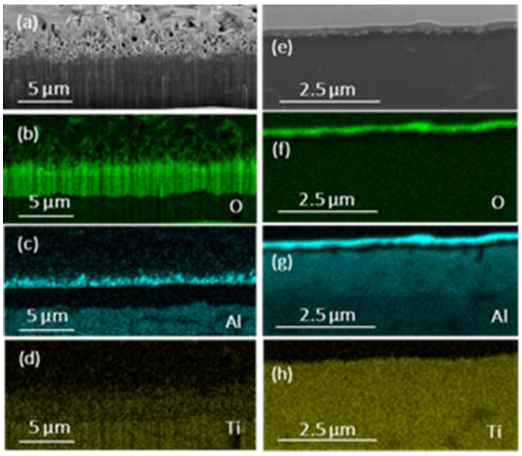

Figure 14. SEM cross-sections and EDS mapping of O, Al, Ti elements of two samples after 5000 h of isothermal oxidation at 600°C: bare Ti6242S (a-d), and DMAI500 coated coupon (e-h). Adapted from [76].

The second example of the use of alumina to meet diverse technological challenges concerns the environmental monitoring. Here, alumina is considered as the matrix component of a nanocomposite film. The work is motivated by the increased needs for environmental monitoring and consequently for robust and reliable sensors. It aims at increasing the service time of optical sensors immersed in riverine waters by decreasing the development of biofouling on their surface. In this aim, nanocomposite coatings composed of metallic silver, Ag nanoparticles (NPs) embedded in alumina are co-deposited on sensor glass windows.[77] The CVD process consists in simultaneously introducing in the process chamber vaporized ATI and direct liquid injected silver pivalate $(CH_3)_3CC(O)OAg$ in the form of a solution in a 90/10 vol. mesytylene/dipropylamine solvent.[78] Co-deposition was performed at 450 °C and 5 Torr. The left part of Figure 15 presents a bright field TEM cross section micrograph of such a coating (15a). It is composed of a 70 nm thick Al_2O_3 sub-layer (2) by the Si substrate (1), followed by a 260 nm thick layer consisting of Ag NPs (black dots) embedded in Al_2O_3 (3). The external part of the coating is composed of a ca. 75 nm thick Al_2O_3 sub-layer (4). In Figure 15b one can observe the Ag NPs. Their size distribution is monodisperse centered at 6 nm. Figure 15c shows a high resolution TEM micrograph of one Ag NP and the insert in this figure reveals the fcc compact stacking of Ag, perfectly oriented in the [111] direction, with a lattice spacing of 0.290 nm between the (110) planes. The right part of Figure 15 presents a phase-contrast image of a 400 × 400 nm^2 surface area. A two scale microstructure, one with ca. 90 nm features size, on the top of which are smaller features, attributed to Ag NPs, whose size does not exceed 10 nm. The quadratic roughness (Sq) of the surface is 5.0 ± 0.5 nm, averaged over 10 images, to be compared with the slightly lower Sq of the bare substrate, 0.8±0.2nm. Such moderate increase of the roughness shouldn't affect the sensor operation and will be taken into account during its calibration phase.

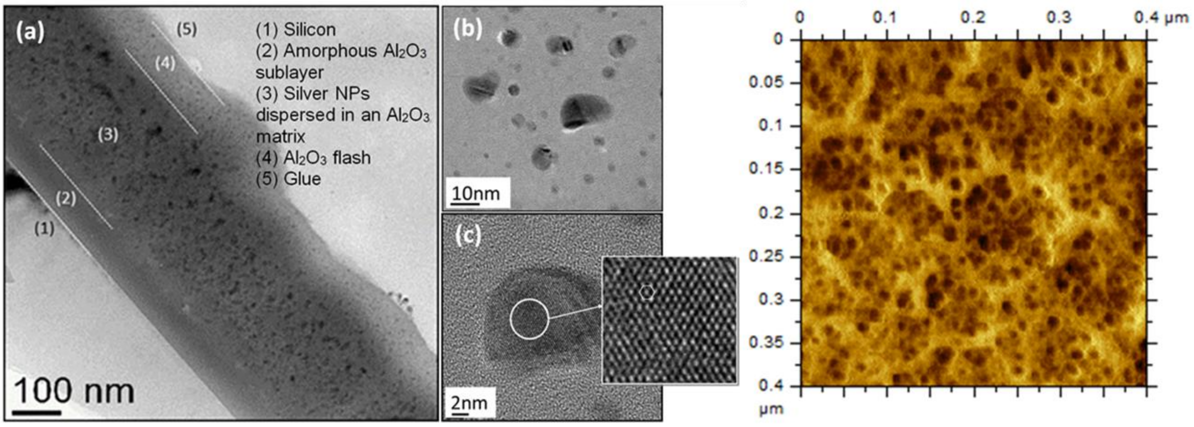

Figure 15. Left: (a) Bright field TEM micrograph of a cross section of a representative amorphous Al_2O_3/Ag NPs composite coating with an alumina rich top-layer, deposited on Si. (b) and (c) High-Resolution TEM micrographs illustrating Ag NPs dispersed in Al_2O_3. The insert in (c) highlights the [111] orientation of an fcc-crystallized Ag NP. The spacing between the (110) reticular planes is 0.290 nm. Right: Atomic force microscopy phase-shift mapping that highlights the contrast between Ag NPs and the Al_2O_3 matrix. Adapted from [77].

Figure 16 summarizes the results of the evaluation of the two targeted functional properties of such films, namely their optical transparency and protection against biofouling. The left part of the Figure shows optical transmittance spectra of four nanocomposite films of increasing thickness from 200 nm (Q4) to 300 nm (Q4). The four dotted lines point on the wavelengths used by the sensor. All four spectra consist of a transmittance band peaking at a fixed position of 315 nm and a broad absorption band covering the vis-NIR spectral domain, which contains several interference fringes. The fixed transmittance band results from the minimum of the imaginary part of the refractive index of bulk Ag k_{Ag}[79] due to Ag interband transitions from 3.83 eV (323 nm) to higher energies.[80] The transmittance band intensity gradually increases from Q1 to Q4, due to the decrease of the film thickness. Thickness increase results in the increase of the absorption since the imaginary part of the resulting effective refractive index of the medium composed of Ag NPs ($k_{Ag} \neq 0$) and Al_2O_3 ($k_{alumina}=0$) host media is non null. Besides, the gradual displacement of the interference fringes towards longer wavelengths is also characteristic of the film thickness increase. The absorption band originates from surface plasmon resonance of Ag NPs which is known to occur between 350 and 800 nm in Al_2O_3 environments.[81, 82] The transmittance at the four wavelengths of interest for sample Q4 is between 0.5 and 0.7. This degradation of the transmittance can be reduced through appropriate tuning of the characteristics of the coating, namely its thickness, and the density and size of the Ag NPs, while maintaining the anti-biofouling efficiency.

The middle part of Figure 16 presents two SEM surface micrographs of bare (Figure 16a) and coated (Figure 16b) glass surfaces after immersion. The observed surfaces confirm visual observations of the samples, namely the complete coverage by microorganisms of the surface of the untreated sample in contrast to the limited, and localized development of biofouling on the surface of the coated one. Quantitative assessment of the biofouling fraction was made by measuring the fraction of bright areas of SEM micrographs of four bare and the four (Q1-

Q4) coated samples by using the using nanoTOPO_SEM™ software (Nanometrisis). The results of the analysis are shown on the top right part of Figure 16 where the biofouling fraction is plotted for various grayscale thresholds (0.4–0.7) used to define the bright areas. In addition to an expected decrease of measured biofouling vs. grayscale threshold, one can notice that, for all grayscale thresholds, the biofouling fraction of coated samples is systematically and unambiguously lower than that of bare samples. To quantify this decrease, we plot the ratio of biofouling of coated to the biofouling of bare samples for four grayscale thresholds, shown in the bottom right diagram of the figure. The value of this ratio is included between 0.30 ± 0.10 and 0.35 ± 0.17; it does not monotonically vary with the value of the grayscale threshold. It is concluded that CVD nanocomposite thin films of Ag NPs embedded in Al_2O_3 are efficient in decreasing biofouling on glass windows.

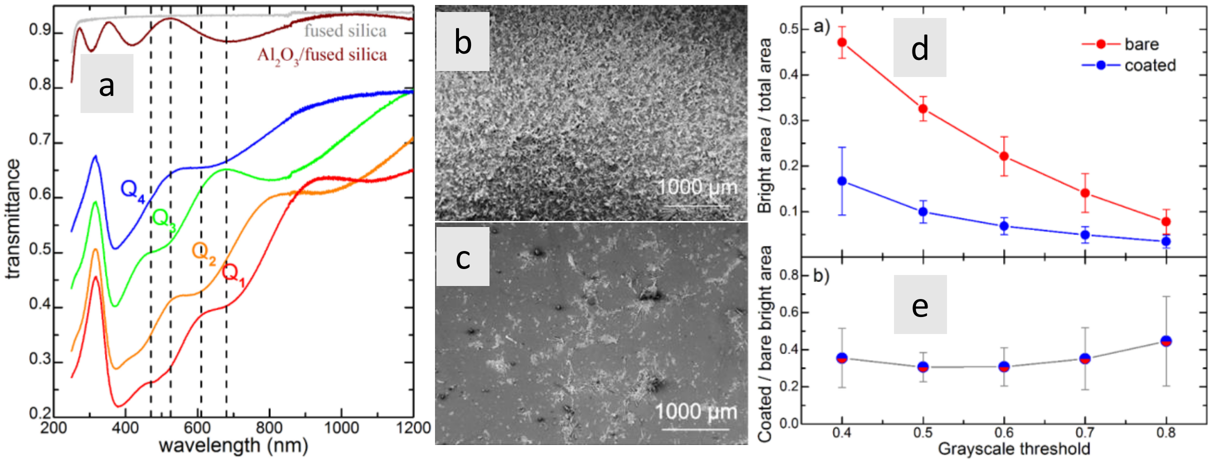

Figure 16. Left (a): Transmittance spectra of four as processed samples composed of Ag NPs doped alumina films co-deposited from ATI and Ag pivalate at 450 °C on commercial sensors glass windows. The thickness of the nanocomposite coatings decreases from Q1 to Q4. Fused silica window and a-Al2O3 deposited on fused silica are shown for comparison. The four dotted lines point on the wavelengths used by the sensor. Middle: SEM surface micrographs of bare (b) and coated (c) glass samples after one-week immersion. Right: Bright area over total area ratios of bare and coated glass samples for a wide range of grayscale thresholds used in the analysis of SEM images (d), coated over bare bright area ratio as a function of the grayscale threefold (b). The error bars indicate the uncertainty of measurements in different images. Adapted from[77].

Concluding remarks

Applied to aluminum oxide thin films, this chapter illustrates the capabilities of the MOCVD process to meet severe requirements of various high-tech industrial fields like microelectronics, photovoltaics, MEMS or anticorrosion barrier layers, to deposit thin films on complex substrates.

Two different and complementary aspects are treated. First, process modelling allows analyzing the interplay between the reactive transport phenomena and the film thickness and composition, in order de develop and optimize new MOCVD processes able to conformally coat complex-in-shape substrates. The second part demonstrates how dedicated multi-criteria experimental studies can correlate the film microstructure and local atomic order to key properties like protection against oxidation and biofouling.

These two generic approaches can be applied to MOCVD thin films of oxides, metals, carbides, nitrides, to coat a great variety of substrates, including patterned wafers, foams, porous media like membranes and even powders.

Acknowledgements : The authors acknowledge A. Gleizes, D. Samelor, D. Sadowski, H. Vergnes, P.L. Etchepare, S. Ponton, C. Tendero, D. Monceau, T. Duguet, V. Turq, R. Laloo for their valuable contribution to the works reported in this chapter.

References

1. Peng, Y.; Han, G. Q.; Liu, F. N.; Xiao, W. W.; Liu, Y.; Zhong, N.; Duan, C. G.; Feng, Z.; Dong, H.; Hao, Y., Ferroelectric-like Behavior Originating from Oxygen Vacancy Dipoles in Amorphous Film for Non-volatile Memory. *Nanoscale Res. Lett.* **2020,** *15* (1), 134.
2. Ryu, H.; Wu, H. N.; Rao, F. B.; Zhu, W. J., Ferroelectric Tunneling Junctions Based on Aluminum Oxide/Zirconium-Doped Hafnium Oxide for Neuromorphic Computing. *Sci. Rep.* **2019,** *9*, 20383.
3. Kaltenbrunner, M.; Stadler, P.; Schwodiauer, R.; Hassel, A. W.; Sariciftci, N. S.; Bauer, S., Anodized Aluminum Oxide Thin Films for Room-Temperature-Processed, Flexible, Low-Voltage Organic Non-Volatile Memory Elements with Excellent Charge Retention. *Adv. Mater.* **2011,** *23* (42), 4892-4896.
4. Silva, J. P. B.; Faita, F. L.; Kamakshi, K.; Sekhar, K. C.; Moreira, J. A.; Almeida, A.; Pereira, M.; Pasa, A. A.; Gomes, M. J. M., Enhanced resistive switching characteristics in Pt/BaTiO3/ITO structures through insertion of HfO2:Al2O3 (HAO) dielectric thin layer. *Sci. Rep.* **2017,** *7*, 46350.
5. Silva, J. P. B.; Sekhar, K. C.; Veltruska, K.; Matolín, V.; Negrea, R.; Ghica, C.; Oliveira, M.; Moreira, J. A.; Castro Pereira, M. A. C.; Gomes, M. J. M., HfO2-Al2O3 dielectric layer for a performing metalferroelectric-insulator-semiconductor structure with ferroelectric 0.5Ba(Zr0.2Ti0.8)O3-0.5(Ba0.7Ca0.3)TiO3 thin film. *ACS Appl. Electron. Mater.* **2020**, *2* (9), 2780-2787.
6. Jang, J.; Song, Y.; Cho, K.; Kim, Y.; Lee, W.; Yoo, D.; Chung, S.; Lee, T., Non-volatile aluminum oxide resistive memory devices on a wrapping paper substrate. *Flexible Printed Electron.* **2016,** *1* (3), 034001.
7. Lazar, A.-M.; Yespica, W. P.; Marcelin, S.; Pébère, N.; Samélor, D.; Tendero, C.; Vahlas, C., Corrosion protection of 304L stainless steel by chemical vapour deposited alumina coatings. *Corros. Sci.* **2014,** *81*, 125-131.
8. Krumdieck, S.; Davies, S.; Bishop, C. M.; Kemmitt, T.; Kennedy, J. V., Al2O3 coatings on stainless steel using pulsed-pressure MOCVD. *Surf. Coat. Technol.* **2013,** *230*, 208-212.
9. Wiest, F.; Capodieci, V.; Blank, O.; Gutsche, M.; Schulze, J.; Eisele, I.; Matusche, J.; Schmidt, U. I., Conformal aluminum oxide coating of high aspect ratio structures using metalorganic chemical vapor deposition. *Thin Solid Films* **2006,** *496* (2), 240-246.

10. Barreca, D.; Battiston, G. A.; Gerbasi, R.; Tondello, E., Al2O3 thin films from aluminium dimethylisopropoxide by metal-organic chemical vapour deposition. *J. Mat. Chem.* **2000,** *10* (9), 2127-2130.

11. Battiston, G. A.; Gerbasi, R., Aluminum dimethylisopropoxide decomposition and the growth of dense alumina thin films at low temperature. *Chem. Vap. Dep.* **2002,** *8* (5), 193-195.

12. Balcaen, Y.; Radutoiu, N.; Alexis, J.; Béguin, J. D.; Lacroix, L.; Samelor, D.; Vahlas, C., Mechanical and barrier properties of MOCVD processed alumina coatings on TA6V titanium alloy. *Surf. Coat. Techn.* **2011,** *206* (7), 1684-1690.

13. Kleijn, C. R.; Dorsman, R.; Kuijlaars, K. J.; Okkerse, M.; van Santen, H., Multi-scale modeling of chemical vapor deposition processes for thin film technology. *J. Cryst. Growth* **2007,** *303* (1), 362-380.

14. Cheimarios, N.; Kokkoris, G.; Boudouvis, A. G., A multi-parallel multiscale computational framework for chemical vapor deposition processes. *J. Computational Sci.* **2016,** *15*, 81-85.

15. Ponton, S.; Vergnes, H.; Samelor, D.; Sadowski, D.; Vahlas, C.; Caussat, B., Development of a Kinetic Model for the Moderate Temperature Chemical Vapor Deposition of SiO2 Films from Tetraethyl Orthosilicate and Oxygen. *AIChE J.* **2018,** *64* (11), 3958-3966.

16. Vergnes, H.; Samelor, D.; Gleizes, A.; Vahlas, C.; Caussat, B., Local kinetic modeling of aluminium oxide MetalOrganic Chemical Vapor Deposition from aluminium tri-isopropoxide. *Chem. Vap. Dep.* **2011,** *17* (7-9), 181–185.

17. Etchepare, P.-L.; Vergnes, H.; Samélor, D.; Sadowski, D.; Caussat, B.; Vahlas, C., Modelling of a DLI MOCVD process to coat by alumina the inner surface of bottles. *Surf. Coat. Technol.* **2015,** *275*, 167–175.

18. Bird, R. B.; Stewart, W. E.; Lightfoot, E. N., *Transport Phenomena*. 2nd ed.; John Wiley & Sons: 2007.

19. Kawase, M.; Ikuta, Y.; Tago, T.; Masuda, T.; Hashimoto, K., Modeling of a thermal gradient chemical vapor infiltration process for production of silicon carbide whisker alumina composite. *Chem. Eng. Sci.* **1994,** *49* (24A), 4861-4870.

20. Kawase, M.; Miura, K., Rate analysis of chemical vapor deposition by use of the thin tubular reactor. *Thin Solid Films* **2006,** *498* (1-2), 25-29.

21. Barybin, A. A.; Tomilin, V. I., Influence of conditions of pyrolysis of triisopropoxyaluminum on certain properties of Al2O3 films. *J. Appl. Chem. USSR* **1976,** *49* (8), 1723-1726.

22. Pauer, G.; Altena, H.; Lux, B., Al2O3 CVD with organic Al-donors. *J. Ref. Hard Metals* **1986,** *Sept.*, 165-170.

23. Hofman, R.; Morssinkhof, R. W. J.; Fransen, T.; Westheim, J. G. F.; Gellings, P. J., *Mat. Manuf. Proc.* **1993,** *8* (3), 315-329.

24. Blittersdorf, S.; Bahlawane, N.; Kohse-Höinghaus, K.; Atakan, B.; Müller, J., Chemical vapor deposition of Al2O3 thin films using aluminium tri-isopropoxide. *Chem. Vap. Deposition* **2003,** *9* (4), 194-198.

25. Saraie, J.; Ono, K.; Takeuchi, S., Effect of various atmospheres on the reduced-pressure CVD of Al_2O_3 thin films at low temperatures. *J. Electrochem. Soc.* **1989,** *136* (10), 3139-3141.

26. Kim, J. H.; Choi, G. J.; Lee, J. K.; Sim, S. J.; Kim, Y. D.; Cho, Y. S., A novel precursor for the sol gel and CVD methods to prepare alumina permselective membranes. *J. Mat. Sci.* **1998,** *33* (5), 1253-1262.

27. Astié, V.; Millon, C.; Decams, J.-M.; Bartasyte, A., Direct Liquid Injection Chemical Vapor Deposition. In *Chemical Vapor Deposition for Nanotechnology*, Mandracci, P., Ed. IntechOpen: London, UK, 2019; pp 29-51.

28. Aboaf, J. A., Deposition and properties of aluminum oxide obtained by pyrolytic decomposition of an aluminum alkoxide. *J. Electroch. Soc.* **1967,** *114* (9), 948-952.

29. Duffy, M. T.; Carnes, J. E.; Richman, D., Dielectric and interface properties of pyrolytic aluminum oxide films on silicon substrates. *Metall. Trans.* **1971,** *2*, 667-672.

30. Okamura, M.; Kobayashi, T., IMPROVED INTERFACE IN INVERSION-TYPE INP-MISFET BY VAPOR ETCHING TECHNIQUE. *Japanese Journal of Applied Physics* **1980,** *19* (11), 2151-2156.

31. Fournier, J.; Desisto, W.; Brusasco, R.; Sosnowski, M.; Kershaw, R.; Baglio, J.; Dwight, K.; Wold, A., Preparation and characterization of thin-films of alumina by metal-organic chemical vapor-deposition. *Mat. Res. Bulletin* **1988,** *23* (1), 31-36.
32. Tanaka, K.; Takahashi, H.; Kuniyoshi, S.; Ohki, H., Electrical-properties of CVD Al2O3-GaAs MIS capacitors. *Solid-State Electron.* **1980,** *23* (10), 1093-1094.
33. Sovar, M. M.; Samélor, D.; Gleizes, A. N.; Alphonse, P.; Perisanu, S.; Vahlas, C., Protective alumina coatings by low temperature metalorganic chemical vapour deposition. *Adv. Mater. Res.* **2007,** *23* 245-248.
34. Gleizes, A.; Sovar, M. M.; Samélor, D.; Vahlas, C., Low temperature MOCVD-processed alumina coatings. *Adv. Sci. Techn.* **2006,** *45*, 1184-1193.
35. Hara, N.; Nagata, S.; Akao, N.; Sugimoto, K., Formation of Al2O3-Ta2O5 double-oxide thin films by low-pressure MOCVD and evaluation of their corrosion resistances in acid and alkali solutions. *Journal of the Electrochemical Society* **1999,** *146* (2), 510-516.
36. Boisier, G.; Raciulete, M.; Samélor, D.; Pébère, N.; Gleizes, A. N.; Vahlas, C., Electrochemical behavior of chemical vapor deposited protective aluminium oxide coatings on Ti6242 titanium alloy. *Electrochem. Sol. State Lett.* **2008,** *11* (10), C55-C57.
37. Morssinkhof, R. W. J.; Fransen, T.; Heusinkveld, M. M. D.; Gellings, P. J., *Mater. Res. Soc. Symp. Proc.* **1990,** *168*, 125.
38. Hofman, R.; Morssinkhof, R. W. J.; Fransen, T.; Westheim, J. G. F.; Gellings, P. J., *Mater. Manuf. Proc.* **1993,** *8*, 315.
39. Haanappel, V. A. C.; van Corbach, H. D.; Hofman, R.; Morssinkhof, R. W. J.; Fransen, T.; Gellings, P. J., Formation of thin oxide films by metal-organic chemical vapor deposition. *High Temp. Mat. Proc.* **1996,** *15* (4), 245-262.
40. Yoshikawa, N.; Takamura, S.; Taniguchi, S.; Kikuchi, A., MOCVD kinetics and morphologies of Al2O3 deposits using aluminium tri-isopropoxide (ATI) precursor. *Trans. Mater. Res. Soc. Jpn.* **1999,** *24*, 151.
41. Gleizes, A.; Vahlas, C.; Sovar, M. M.; Samélor, D.; Lafont, M. C., CVD-Fabricated Aluminum Oxide Coatings from Aluminum tri-iso-propoxide: Correlation Between Processing Conditions and Composition. *Chem. Vap. Dep.* **2007,** *13*, 23-29.
42. Sovar, M. M.; Samélor, D.; Gleizes, A. N.; Vahlas, C., Aluminium tri-isopropoxide: shelf life, transport properties, and decomposition kinetics for the low temperature processing of aluminium oxide-based coatings. *Surf. Coat. Techn.* **2007,** *201* 9159-9162.
43. Maruyama, T.; Nakai, T., Aluminum oxide thin films prepared by chemical vapor deposition from aluminum 2-ethylhexanoate. *Appl. Phys. Lett.* **1991,** *58* (19), 2079-2080.
44. Haanappel, V. A. C.; Rem, J. B.; Vancorbach, H. D.; Fransen, T.; Gellings, P. J., Properties of alumina films prepared by metal-organic chemical vapor deposition at atmospheric pressure in the presence of small amounts of water. *Surf. Coat. Techn.* **1995,** *72* (1-2), 1-12.
45. Haanappel, V. A. C.; Vendel, D. v. d.; Metselaar, H. S. C.; Corbach, H. D. v.; Fransen, T.; Gellings, P. J., The mechanical properties of thin alumina films deposited by metal-organic chemical vapour deposition. *Thin Solid Films* **1995,** *254*, 153-163.
46. Kuo, D.-H.; Cheung, B.-Y.; Wu, R.-J., Growth and properties of alumina films obtained by low-pressure metal-organic chemical vapor deposition. *Thin Solid Films* **2001,** *398-399*, 35-40.
47. Ajayi, O. B.; Akanni, M. S.; Lambi, J. N.; Burrows, H. D.; Osasona, O.; Podor, B., Preparation and optical characterization of pyrolytically deposited thin films of some metal oxides. *Thin Solid Films* **1986,** *138* (1), 91-95.
48. Ajayi, O. B.; Akanni, M. S.; Lambi, J. N.; Jeynes, C.; Watts, J. F., Compositional studies of various metal oxide coatings on glass. *Thin Solid Films* **1990,** *185* (1), 123-136.
49. Pulver, M.; Nemetz, W.; Wahl, G., CVD of ZrO2, Al2O3 and Y2O3 from metalorganic compounds in different reactors. *Surf. Coat. Techn.* **2000,** *125* (1-3), 400-406.
50. Battiston, G. A.; Carta, G.; Cavinato, G.; Gerbasi, R.; Porchia, M.; Rossetto, G., MOCVD of Al2O3 films using new dialkylaluminum acetylacetonate precursors: Growth kinetics and process yields. *Chem. Vap. Dep.* **2001,** *7* (2), 69-74.

51. Koh, W.; Ku, S.-J.; Kim, Y., Chemical vapor deposition of A1203 films using highly volatile single sources. *Thin Solid Films* **1997,** *304* (1-2), 222-224.

52. Lee, S. Y.; Luo, B.; Sun, Y.; White, J. M.; Kim, Y., Thermal decomposition of dimethylaluminum isopropoxide on Si(1 0 0). *Appl. Surf. Sci.* **2004,** *222* (1-4), 234-242.

53. Natali, M.; Carta, G.; Rigato, V.; Rossetto, G.; Salmaso, G.; Zanella, P., Chemical, morphological and nano-mechanical characterizations of Al2O3 thin films deposited by metal organic chemical vapour deposition on AISI 304 stainless steel. *Electrochim. Acta* **2005,** *50* (23), 4615-4620.

54. Guidi, F.; Moretti, G.; Carta, G.; Natali, M.; Rossetto, G.; Pierino, Z.; Salmaso, G.; Rigato, V., Electrochemical anticorrosion performance evaluation of Al2O3 coatings deposited by MOCVD on an industrial brass substrate. *Electrochim. Acta* **2005,** *50* (23), 4609-4614.

55. Carta, G.; Casarin, M.; El Habra, N.; Natali, M.; Rossetto, G.; Sada, C.; Tondello, E.; Zanella, P., MOCVD deposition of CoAl2O4 films. *Electrochim. Acta* **2005,** *50* (23), 4592-4599.

56. Schmidt, B. W.; Rogers, B. R.; Gren, C. K.; Hanusa, T. P., Carbon incorporation in chemical vapor deposited aluminum oxide films. *Thin Solid Films* **2010,** *518* (14), 3658-3663.

57. Baggetto, L.; Charvillat, C.; Esvan, J.; Thébault, Y.; Samélor, D.; Vergnes, H.; Caussat, B.; Gleizes, A.; Vahlas, C., A process-structure investigation of aluminum oxide and oxycarbide thin films prepared by direct liquid injection chemical vapor deposition of dimethylaluminum isopropoxide (DMAI). *Chem. Vap. Dep.* **2015,** *21*, 343-351.

58. Manin, M.; Thollon, S.; Emieux, F.; Berthome, G.; Pons, M.; Guillon, H., Deposition of MgO thin film by liquid pulsed injection MOCVD. *Surf. Coat. Techn.* **2005,** *200* (5-6), 1424-1429.

59. Mungkalasiri, J.; Bedel, L.; Emieux, F.; Doré, J.; Renaud, F. N. R.; Maury, F., DLI-CVD of TiO2–Cu antibacterial thin films: Growth and characterization. *Surf. Coat. Techn.* **2009,** *204* (6-7), 887-892.

60. Etchepare, P.-L.; Vergnes, H.; Samélor, D.; Sadowski, D.; Brasme, C.; Caussat, B.; Vahlas, C., Amorphous alumina coatings on glass bottles using direct liquid injection MOCVD for packaging applications. *Adv. Sci. Techn.* **2014,** *91*, 117-122.

61. Vahlas, C.; Caussat, B.; Gladfelter, W. L.; Senocq, F.; Gladfelter, E. J., Liquid and solid precursor delivery systems in gas phase processes. *Recent Patents on Complex Metallic Alloys* **2015,** *8*, 91-108.

62. Etchepare, P.-L.; Baggetto, L.; Vergnes, H.; Samélor, D.; Sadowski, D.; Caussat, B.; Vahlas, C., Amorphous Alumina Barrier Coatings on Glass: MOCVD Process and Hydrothermal Aging. *Adv. Mater. Interf.* **2016,** *3* (8), 1600014.

63. Baggetto, L.; Esvan, J.; Charvillat, C.; Samélor, D.; Vergnes, H.; Caussat, B.; Gleizes, A.; Vahlas, C., Alumina thin films prepared by direct liquid injection chemical vapor deposition of dimethylaluminum isopropoxide: a process-structure investigation. *Phys. Status Solidi C* **2015,** *12* (7), 989-995.

64. Schmidt, B. W.; Rogers, B. R.; Sweet Iii, W. J.; Gren, C. K.; Hanusa, T. P., Deposition of alumina from dimethylaluminum isopropoxide. *J. Eur. Cer. Soc.* **2010,** *30* (11), 2301-2304.

65. Sarou-Kanian, V.; Gleizes, A. N.; Florian, P.; Samelor, D.; Massiot, D.; Vahlas, C., Temperature-Dependent 4-, 5- and 6-Fold Coordination of Aluminum in MOCVD-Grown Amorphous Alumina Films: A Very High Field Al-27-NMR study. *J. Phys. Chem. C* **2013,** *117* (42), 21965-21971.

66. Lee, S. K.; Lee, S. B.; Park, S. Y.; Yi, Y. S.; Ahn, C. W., Structure of amorphous aluminum oxide. *Phys. Rev. Lett.* **2009,** *103*, 095501.

67. Lee, S. K.; Park, S. Y.; Yi, Y. S.; Moon, J., Structure and Disorder in Amorphous Alumina Thin Films: Insights from High-Resolution Solid-State NMR. *J. Phys. Chem. C* **2010,** *114* (32), 13890-13894.

68. Baggetto, L.; Sarou-Kanian, V.; Florian, P.; Gleizes, A. N.; Massiot, D.; Vahlas, C., Atomic Scale Structure of Amorphous Aluminum Oxyhydroxide, Oxide and Oxycarbide Films Probed by Very High Field 27Al Nuclear Magnetic Resonance. *Phys.Chem.Chem.Phys.* **2017,** *19*, 8101-8110.

69. Samélor, D.; Lazar, A. M.; Aufray, M.; Tendero, C.; Lacroix, L.; Béguin, J. D.; Caussat, B.; Vergnes, H.; Alexis, J.; Poquillon, D.; Pébère, N.; Gleizes, A.; Vahlas, C., Amorphous alumina coatings : processing, structure and remarkable barrier properties. *J. Nanosci. Nanotech.* **2011,** *11* (9), 8387-8391.

70. Samélor, D.; Aufray, M.; Lacroix, L.; Balcaen, Y.; Alexis, J.; Vergnes, H.; Poquillon, D.; Beguin, J. D.; Pébère, N.; Marcelin, S.; Caussat, B.; Vahlas, C., Mechanical and surface properties of chemical vapour deposited protective aluminium oxide films on TA6V alloy. *Adv. Sci. Techn.* **2010,** *66*, 66-73.

71. Lütjering, G.; Williams, J. C., *Titanium*. Springer-Verlag: Berlin, Heidelberg, 2007.

72. Shenoy, R. N.; Unnam, J.; Clark, R. K., Oxidation and embrittlement of Ti-6Al-2Sn-4Zr-2Mo alloy. *Oxid. Met.* **1986,** *26* (1-2), 105-124.

73. Dupressoire, C.; Rouaix-Vande Put, A.; Emile, P.; Archambeau-Mirguet, C.; Peraldi, R.; Monceau, D., Effect of Nitrogen on the Kinetics of Oxide Scale Growth and of Oxygen Dissolution in the Ti6242S Titanium-Based Alloy. *Oxid. Met.xia* **2017,** *87* (3-4), 343-353.

74. Monceau, D.; Poquillon, D., Continuous thermogravimetry under cyclic conditions. *Oxid. Met.* **2004,** *61* (1-2), 143-163.

75. Brumm, M. W.; Grabke, H. J., The oxidation behaviour of NiAl - I.Phase transformations in the alumina scale during oxidation of NiAl and NiAl-Cr alloys. *Corros. Sci.* **1992,** *33* (11), 1677-1690.

76. Samelor, D.; Baggetto, L.; Laloo, R.; Turq, V.; Gleizes, A. N.; Duguet, T.; Monceau, D.; Vahlas, C., Efficient, durable protection of the Ti6242S titanium alloy against high-temperature oxidation through MOCVD processed amorphous alumina coatings. *J. Mat. Sci.* **2020,** *55* (11), 4883-4895.

77. Tendero, C.; Lazar, A. M.; Samelor, D.; Debieu, O.; Constantoudis, V.; Papavieros, G.; Villeneuve, A.; Vahlas, C., Nanocomposite thin film of Ag nanoparticles embedded in amorphous Al2O3 on optical sensors windows: Synthesis, characterization and targeted application towards transparency and anti-biofouling. *Surf. Coat. Technol.* **2017,** *328*, 371-377.

78. Mungkalasiri, J.; Bedel, L.; Emieux, F.; Dore, J.; Renaud, F. N. R.; Sarantopoulos, C.; Maury, F., CVD Elaboration of Nanostructured TiO_2-Ag Thin Films with Efficient Antibacterial Properties. *Chem. Vap. Dep.* **2010,** *16*, 35-41.

79. Meng, X. K.; S.C., T.; Vongehr, S., A Review on Diverse Silver Nanostructures. *J. Mater. Sci. Technol.* **2010,** *26* (6), 487-522.

80. Fox, M., Introduction to Nanophotonics, Sergey V. Gaponenko. *Contemporary Physics* **2011,** *52* (3), 257.

81. Camelio, S.; Vandenhecke, E.; Rousselet, S.; Babonneau, D., Optimization of growth and ordering of Ag nanoparticle arrays on ripple patterned alumina surfaces for strong plasmonic coupling. *Nanotechnology* **2014,** *25*, 035706.

82. Esteban-Cubillo, A.; Dıaz, C.; Fernandez, A.; Dıaz, L. A.; Pecharroman, C., Silver nanoparticles supported on α–, η-, and δ-alumina. *J. Eur. Cer. Soc.* **2006,** *26*, 1-7.